Structural snapshots of base excision by the cancer-associated variant MutY N146S reveal a retaining mechanism

Merve Demir,[1] L. Peyton Russelburg,[2] Wen-Jen Lin,[1] Carlos H. Trasvina-Arenas,[1] Beili Huang,[1] Phil K. Yuen,[1] Martin P. Horvath,[2,*] and Sheila S. David[1,*]

[1] Department of Chemistry, University of California, Davis, California, 95616, USA

[2] School of Biological Sciences, University of Utah, Salt Lake City, Utah, 84112, USA

* To whom correspondence should be addressed. Email: ssdavid@ucdavis.edu; martin.horvath@utah.edu

ABSTRACT

DNA glycosylase MutY plays a critical role in suppression of mutations resulted from oxidative damage, as highlighted by cancer-association of the human enzyme. MutY requires a highly conserved catalytic Asp residue for excision of adenines misinserted opposite 8-oxo-7,8-dihydroguanine (OG). A nearby Asn residue hydrogen bonds to the catalytic Asp in structures of MutY and its mutation to Ser is an inherited variant in human MUTYH associated with colorectal cancer. We captured structural snapshots of N146S Geobacillus stearothermophilus MutY bound to DNA containing a substrate, a transition state analog and enzyme-catalyzed abasic site products to provide insight into the base excision mechanism of MutY and the role of Asn. Surprisingly, despite the ability of N146S to excise adenine and purine (P) *in vitro*, albeit at slow rates, N146S-OG:P complex showed a calcium coordinated to the purine base altering its conformation to inhibit hydrolysis. We obtained crystal structures of N146S Gs MutY bound to its abasic site product by removing the calcium from crystals of N146S-OG:P complex to initiate catalysis in crystallo or by crystallization in the absence of calcium. The product structures of N146S feature enzyme-generated β-anomer abasic sites that support a retaining mechanism for MutY-catalyzed base excision.

INTRODUCTION

The DNA glycosylase MutY prevents accumulation of G:C to T:A transversion mutations resulting from oxidation of guanine (G) to 8-oxo-7,8-dihydroguanine (OG) (1). During DNA replication, the *syn* conformer of OG directs the misincorporation of adenine to form stable OG:A mispairs that evade fidelity mechanisms of the replicative polymerases (2). MutY (MUTYH in humans) recognizes OG:A mispairs and removes the undamaged adenine as the first step in restoration of G:C base pairs (bps) through base excision repair (BER). Failure to repair OG:A mispairs by inherited variants of MUTYH has been linked to the colorectal cancer predisposition syndrome MUTYH-associated Polyposis (MAP) (3, 4). Providing a structural and mechanistic rationale for MAP variant dysfunction and magnitude has been a major impetus for fully elaborating molecular features of OG:A recognition and A excision by MutY enzymes.

Insight into the adenine excision mechanism of MutY has been gleaned through site-directed mutagenesis, kinetic isotope effect measurements, X-ray crystallography and stereochemical determination of methanolysis products (5–9). Taken together, the available information indicates an S_N1-like mechanism for MutY with retention of stereochemistry, reminiscent of mechanisms proposed for “retaining” O-glycosidases (**Figure 1A**) (10–12). Key features of the most up-to-date mechanism are protonation of N7 of adenine by the catalytic glutamic acid residue (Glu43 in *Gs* MutY), and formation of a transient covalent intermediate with the catalytic residue Asp144 to C1’ of the deoxyribose sugar to stabilize the oxacarbenium ion as the base departs (7). The transient acetal intermediate is hydrolyzed by a water nucleophile activated by Glu43 to form the abasic site product. Despite the acceptance of such mechanisms for O-glycosidases, similar retaining mechanisms have not been widely considered for BER N-glycosylases (**Figure 1A**).

Structural inspiration for a retaining MutY mechanism originated from the X-ray crystal structure of DNA containing a pyrrolidine transition state analog (TSA), 1N, complexed with thermophilic *Geobacillus*

stearothermophilus (*Gs*) MutY (TSAC-OG:1N, PDB ID 6U7T) (7). In the TSAC-OG:1N structure, the catalytic residue Asp144 was shown to be in close contact with N1' of 1N (**Figure 1B&C**), and a water molecule was positioned on the opposite side interacting with the catalytic Glu43 residue. Conspicuously, the active site residue Asn146 is proximal to Asp144, suggesting a role as a "second sphere" modulator of catalytic activity by aligning and tuning the Asp144 nucleophile (6, 7). In addition, Asn146 interacts with the 5' phosphate group of the target nucleotide suggesting roles in positioning the substrate for catalysis. Notably, mutation of Asn146 to a serine corresponds to MAP variant N238S in MUTYH (13, 14). The prominent positioning of Asn146, and the correlation with mutations at this position in MUTYH in MAP, suggested to us that N146S *Gs* MutY may be leveraged to unveil new structural insights into the MutY mechanism.

Herein, we report detailed *in vitro* kinetics and binding experiments of N146S *Gs* MutY (or the equivalent variant in *E. coli* MutY; N140S), along with several X-ray crystal structures with DNA substrate, transition state mimic and enzyme-generated abasic (apurinic/apyrimidinic; AP) product. N146S *Gs* MutY and N140S *Ec* MutY retained activity with OG:A substrates and with an alternative substrate OG:P (where P = purine) (**Figure 1C**), albeit significantly reduced compared to the wild type (WT) enzyme. The structure of N146S *Gs* MutY bound to the transition state analog OG:1N was nearly identical to that of the WT enzyme with increased distances of the introduced Ser to Asp144 and the phosphate of the DNA, consistent with removal of key H-bonds originally established with side chain of Asn146. Unexpectedly, we captured N146S *Gs* MutY in complex with the OG:P substrate with the N-glycosidic linkage to purine intact. The replacement of Asn with the Ser residue allowed a Ca^{2+} ion to coordinate to the substrate in the active site and apparently inhibit excision of the base. We obtained structures of N146S *Gs* MutY bound to its enzyme-catalyzed OG:AP site product using three different strategies: (1) replacement of Ca^{2+} with Na^{+} during crystallization, (2) addition of Ca^{2+} to the reaction mixture incubated for an extended time and (3) soaking the trapped substrate complex crystals in EGTA containing solution for Ca^{2+} removal. All product structures revealed formation of the β anomer AP site consistent with retention of configuration that significantly extends support for a double-displacement mechanism involving catalytic residues Asp144 and Glu43.

MATERIAL AND METHODS

Oligonucleotide synthesis and purification

The (3R,4R)-3-hydroxy-4-(hydroxymethyl) pyrrolidine-1-ium phosphoramidite (1N) was synthesized as previously described (15). The phosphoramidites of 8-oxo-dG, 2'-F-A and 2'-DeoxyNebularine were purchased from Glen Research. The commercially available FA phosphoramidite that constitutes the ribo configuration of the fluorosugar was used in the binding experiments. The 1N, OG (8-oxo-7,8- dihydroguanosine), A, FA (2'-deoxy-2'-fluoro-adenosine) and Purine (2'-deoxynebularine) containing oligonucleotides were synthesized at the University of Utah core facility. OG-containing oligonucleotides were cleaved from the column and deprotected using ammonium hydroxide with 0.25 M β-mercaptoethanol for 17 hours at 55 °C. All oligonucleotides were HPLC purified using Dionex ion

exchange column and desalted with a Sep-Pak C18 desalting cartridge (Waters). Oligonucleotide integrity was confirmed by matrix-assisted laser-desorption/ionization (MALDI) mass spectrometry at the UC Davis Mass Spectrometry Facility:

Duplex 1 (5'-TGTCCA**X**GTCT-3':3'-CAGGT**Y**CAGAA-5') where X is 1N or P and Y is OG. Duplex 2 (5'-CTGTAACGGGAGCT**X**GTGGCTCCATGATCG-3':3'-GACATTGCCCTCGA**Y**CACCGAGGTACTAGC-5') where X is A, P or FA and Y is OG.

Enzyme Preparation

The single point N146S and N140S mutations in *Gs* MutY and *Ec* MutY respectively were created using ligation independent cloning with PCR primers (16, 17). The pET28a vector encoding either WT or N146S *Geobacillus stearothermophilus* (*Gs*) MutY with N-terminal His6-tag were overexpressed at 30 °C in BL21(DE3) Rosetta II *E. coli* cell lines transformed with the pRKISC plasmid that encodes iron-sulfur cluster cofactor assembly proteins (18). *Gs* MutY was purified using Ni^{+2}-NTA (Qiagen), MonoQ (GE Healthcare) and Superdex 200 (GE healthcare) chromatography columns as similarly described previously (7, 19). Tagless N140S *Ec* MutY in pKK223 vector was overexpressed in JM101 mutY^{-} *E. coli* cells and purified as previously described (20). The crude extract was separated from nucleic acids by streptomycin sulfate precipitation which was followed by precipitation of proteins with 40% ammonium sulfate. N140S variant was then further purified by using HiPrep 26/10 desalting (Pharmacia), HiTrap SP HP cation-exchange (GE healthcare), and HiTrap Heparin HP cation exchange (GE healthcare).

Determination of Glycosylase Activity

The rate constants for *Gs* and *Ec* MutY were measured by using previously described glycosylase assay methods (21). To determine the rate constant of adenine removal, k_2, and the rate constant describing product release, k_3, a 30 base pair Duplex 2 with a central OG:A mismatch was utilized. The 5'-end of the A-containing strand is radiolabeled using γ-^{32}P-ATP and T4 Polynucleotide Kinase (NEB) and annealed to its complementary strand containing OG in a buffer solution containing 20 mM Tris pH 7.6, 10 mM EDTA and 150 mM sodium chloride. The 20 nM duplex was incubated with enzyme at 60 °C for *Gs* and 37 °C for *Ec* MutY with final reaction conditions of 20 mM Tris pH 7.6, 10 mM EDTA, 0.1 mg/mL bovine serum albumin (BSA) and 30 mM NaCl. Reactions were performed at 60°C since the thermophilic homolog *Gs* MutY has optimal activity at higher temperatures (22). The aliquot removed from the reaction at certain time points is quenched with sodium hydroxide to introduce a single DNA strand break at the abasic site forming a 14-nucleotide (nt) product strand. The unprocessed 30-nt substrate strand is separated from the product strand using a denaturing PAGE for quantification. A rapid quench flow instrument (Kintek) was used for reactions faster than that can be measured with manual kinetics where k_2>2 min^{-1}. Enzyme concentrations of 4, 8 and 12 nM were used for glycosylase assays performed under multiple turnover conditions to measure k_3 values. The rate constant of adenine removal, k_2, was measured under single turnover (STO) conditions using enzyme concentrations of 120 nM for WT *Gs*, 100 nM for N146S *Gs*, 40 nM for WT *Ec* and 100 nM for N140S *Ec* MutY. The metal inhibition test was performed using glycosylase assays under STO conditions with 30 min reaction incubation of OG:A containing radiolabeled DNA with

excess enzyme. To obtain the pH profiles of WT and N146S *Gs* MutY, the glycosylase assay was performed at each pH condition in the range of 4-10.5 with final reaction conditions of 20 mM pH buffer, 5 mM EDTA, 0.1 mg/mL bovine serum albumin (BSA) and 30 mM sodium chloride (23). Sodium acetate was used as a buffer in the reaction for pH range of 4-5.5, MES for 5.5-6.5 and Tris-HCl for pH conditions higher than 6.5 as previously described for *Ec* MutY. The slow rates at pH 4 for N146S were calculated from the initial rates of three time points.

Electrophoretic mobility shift assay (EMSA)

The DNA binding affinity was measured by using electrophoretic mobility shift assays (EMSA) for *Ec* MutY using previously described procedures (24). The 5'-end of radiolabeled 2'-F-A containing strand was annealed to its complementary strand with OG and a DNA master mix was prepared in buffer containing 40 mM Tris pH 7.6, 2 mM EDTA, 200 M sodium chloride, 20% (w/v) glycerol, 0.2 mg/mL BSA, 2 mM DTT and 20 pM of radiolabeled Duplex 2. Equal volumes of DNA master mix were combined with enzyme in decreasing concentrations (prepared at 4°C in dilution buffer containing 20 mM Tris pH 7.6, 10 mM EDTA and 20% glycerol) and incubated for 30 min at 25 °C. The enzyme bound DNA was separated from the unbound DNA using 6% nondenaturing polyacrylamide gel ran with 0.5X TBE buffer at 120 V for 2 hr at 4 °C. The gels were dried and quantified, and the data was fit to single binding isotherm model to derive the dissociation constant, K_D.

Crystallization and Structure Determination

Crystals of MutY complexed to DNA were obtained by hanging-drop vapor diffusion complemented by micro-seeding. Typically, N146S *Gs* MutY was mixed in equal volume with Duplex 1 and incubated for 30 min at room temperature to yield a final solution comprising 175 μM protein, 263 μM DNA, 15 mM Tris pH 7.6, 100 mM sodium chloride and 2.5 mM β-mercaptoethanol. Crystallization well solutions consisted of 100 mM Tris pH 8.5, 14% (w/v) PEG 4000, 500 mM calcium acetate, 2% (v/v) ethylene glycol, and 5 mM β-mercaptoethanol. The Ca-free crystals were obtained with crystallization solutions containing 100 mM Tris pH 8.0, 29% (w/v) PEG 4000 and 250 mM sodium acetate, a condition previously described in the literature for MutY crystallization (25). Crystals grew from reactions prepared by mixing 1 μL MutY-DNA with 1 μL well solution containing microcrystals prepared from crystals previously obtained from similar conditions (26). Golden brown crystals appeared as rods or plates within a few days at room temperature. Crystals were harvested directly from drops or washed briefly in a solution matching the reservoir conditions prior to freezing in liquid nitrogen. The Ca-depleted (N146S-OG:$AP_{Ca\text{-}depleted}$) crystals were rinsed in small 10-uL drops of EGTA-containing solutions, soaking for at least 5 min, and serially moving the crystal from one drop to the next, for a total of three rinsing steps, before final incubation for one week in a 2 mL solution containing 100 mM Tris pH 8.0, 14% (w/v) PEG 4000, 100 mM sodium acetate, 2% (v/v) ethylene glycol and 200 mM EGTA. X-ray diffraction data were collected at the Advanced Light Source beamlines 8.3.1 and 5.0.1. The diffraction data were indexed, scaled and merged with the XDS package, keeping Friedel Mates separate so as to be able to detect metal ions (27). Initial phases were generated from rigid body refinement with published and unpublished structures of MutY in complex with DNA. Refinement of the

structures was performed in PHENIX with model adjustments in Coot guided by $2|F_o| - |F_c|$, $|F_o| - |F_c|$ and anomalous difference maps interleaved with each cycle of refinement (28–30). Refinement included at least one round of torsion-angle simulated annealing with a starting temperature of 2200-2500 K, and several repeats of positional refinement together with individual B-factor and occupancy optimizations. At the final stage, parameters describing a limited number of TLS groups for the N-terminal domain, C-terminal domain, and DNA were included for those models that benefited from anisotropic temperature factors as evidenced by a significant drop in R_{free} larger than 0.8%. Supplementary Table S1 and Table S2 contain the detailed data collection and model refinement statistics. Figures of the structures were prepared using UCSF Chimera (31). The movie was made with UCSF ChimeraX (32). Structures were deposited at the Protein Data Bank with PDB ID: 8DVP, 8DW7, 8DW0, 8DVY, 8DW4.

RESULT AND DISCUSSION

Impact on kinetic and binding parameters of Asn to Ser in *Gs* and *Ec* MutY

We anticipated that the Asn-to-Ser substitution would impact MutY-catalyzed base excision based on the prominent positioning of Asn146 in the *Gs* MutY-DNA structures. The catalytic activity of N146S *Gs* MutY and N140S *Ec* MutY variants was analyzed using gel-based glycosylase assays under single and multiple-turnover conditions (21). Both N146S *Gs* MutY and N140S *Ec* MutY displayed "burst" kinetics under multiple turnover (MTO) conditions ([DNA] > [MutY]) due to rate-limiting product release as observed with WT ((k_3<k_2), **Scheme 1**). Therefore, we used an analogous approach to determine rate constants for the variants, relating to product release (k_3) and all steps from E-S to E-P (**Scheme 1**) including N-glycosidic bond hydrolysis (k_2) (**Scheme 1**) (7, 21). The product release rate constant (k_3) determined under MTO conditions showed that N146S *Gs* MutY releases the AP-site product approximately 3-fold slower than WT (Table 1). The rate constant for adenine excision (k_2) was measured under single turnover conditions ([MutY] > [DNA] and K_D, **Table 1**). Specifically, the rate constant k_2 for adenine excision across OG with N146S *Gs* MutY at 60 °C was ~180-fold reduced relative to WT *Gs* MutY. Similarly, N140S *Ec* MutY had a ~70-fold decrease in adenine removal at 37 °C with the OG:A substrate compared to WT *Ec* MutY (**Table 1**). The dissociation constant (K_D) measured by EMSA of N140S *Ec* MutY with a radiolabeled 30 bp DNA duplex containing a non-cleavable substrate analog FA across OG, was comparable to that of WT (**Figure 2**). This finding is consistent with previous work that has shown the high affinity of MutY for its substrates and products is dominated by interactions of the C-terminal domain with OG (33–35). Of note, the determination of DNA binding affinity using EMSA has not been successful for *Gs* MutY; hence we determined the K_D of *Ec* MutY for comparison. Taken together, the functional assays indicate that the reduced activity resulting from the Asn-to-Ser substitution arises mainly from altering chemical step(s) of base excision, rather than overall DNA substrate affinity.

Next, we tested the glycosylase activity of N146S *Gs* MutY and N140S *Ec* MutY with DNA containing a substrate, purine (P), across OG, with the goal of slowing steps in catalysis to potentially capture intermediates and glean new mechanistic insights. The purine substrate is structurally similar to

adenine except for the lack of exocyclic amino group that alters base-pairing with OG, as well as potential contacts within the MutY active site. Purine has been previously reported to show a higher acid lability than adenine and is excised only ~2-fold slower than adenine by WT *Ec* MutY (33, 35) with a product release rate of 0.003 ± 0.001 min^{-1} (33). In contrast, the rate constants k_2 for purine removal by N146S *Gs* MutY and N140S *Ec* MutY revealed a much more dramatic reduction in the activities by ~92-fold and ~200-fold in comparison to the respective WT enzymes (**Table 1, Figure 2A&B**). The product release rate for the variants was not measurable due to lack of burst kinetics ($k_3 \lesssim k_2$). The higher selectivity for adenine relative to purine for WT *Gs* MutY (49-fold) over N146S (25-fold) highlights the potential significance of the interaction between the exocyclic amino group of adenine and Glu188 observed in the Fluorinated Lesion Recognition Complex (FLRC, PDB ID: 3G0Q) structure (6). Moreover, these results show that minor structural alterations from the preferred natural substrate adenine are even less well-tolerated combined with mutations in the active site and further underscore a key role of Asn146 in base-excision steps of catalysis. The ability to further slow catalysis with the OG:P substrate suggested its use in strategies to capture new *Gs* MutY-DNA complex structures.

Strategies for Capturing Structural Snapshots of N146S *Gs* MutY

To understand the structural basis for impaired catalytic performance, we crystallized N146S *Gs* MutY in complex with several different DNAs (**Figure 3A**). Herein, we present three classes of structures for the *Gs* MutY variant N146S in complex with DNA containing mechanistically distinct moieties: (1) substrate (purine), (2) transition state analog (1N) and (3) abasic site product (AP). As demonstrated here, N146S *Gs* MutY has reduced glycosylase activity, especially when adenine is replaced with purine, suggesting that purine would be a suitable candidate for crystallization to obtain a substrate, an intermediate or a product structure of MutY. The incubation of OG:P containing DNA with the enzyme for 30 min and mixing the complex with Ca^{2+} containing crystallization solution resulted in capturing the structure in the first class with intact purine substrate, referred to as N146S-OG:P. Crystals belonging to this substrate class grew in the familiar $P2_12_12_1$ space group, diffracted synchrotron radiation to very high resolution, and the structure we are reporting refined to the 1.54 Å resolution limit. The high-resolution structure of N146S-OG:P revealed interesting new features of the enzyme with a Ca^{2+} ion coordinated in the active site inhibiting excision of purine by positioning the target base in an unproductive conformation.

For the second structure class, we used duplex DNA containing the azaribose transition state analog (3R,4R)-4-(hydroxymethyl)pyrrolidine-3-ol (1N) that exhibits exceptionally high affinity for MutY enzymes by mimicking the shape and charge of the oxacarbenium ion transition state and intermediate (7, 15, 36). We captured the structure of N146S complexed to the OG:1N transition state analog containing DNA using the same calcium containing crystallization conditions as for OG:P substrate duplex (**Figure 3B**). Crystals belonging to the transition state analog class grew in the $P2_1$ space group with two enzyme-DNA complexes in the asymmetric unit and diffracted synchrotron radiation to the 1.9 Å resolution limit. The refined structure, referred to as N146S-OG:1N, showed stabilizing interactions highly comparable to those

previously described for wild-type *Gs* MutY, except that the hydrogen bond between the residue at position 146 and Asp 144 is absent.

Finally, we obtained several structures belonging in the third class with N146S *Gs* MutY in complex with the enzyme-generated abasic (apurinic/apyrimidinic, AP) site. Crystals belonging in this AP site product class all grew in the $P2_12_12_1$ space group and diffracted synchrotron radiation to varying resolution limits ranging from 1.68 to 2.49 Å. Three structures were fully refined, each generated by a different strategy starting from OG:P containing DNA, and each with important implications for mechanistic interpretation. As described further below, divalent metal ions, such as calcium ions included in crystallization reactions for many MutY crystal structures, inhibit the enzyme (**Figure S1**). We leveraged this metal-ion inhibition to control the timing of crystal formation relative to start or termination of the enzyme-catalyzed base excision reaction. In the first strategy, we incubated the enzyme-DNA mixture for 3 days at room temperature to allow sufficient time for full conversion of substrate to product. Indeed, using this strategy, we trapped N146S in a complex with ring-closed abasic (AP) product coordinated to a Ca^{2+} ion with no evidence of an intact purine N-glycosidic bond or free purine base in the active site indicating full conversion of substrate to product (**Figure 3C**). We will refer to this AP product structure prepared with long incubation time and calcium inhibition as AP-calcium-inhibited (N146S-OG:$AP_{Ca\text{-}inhibited}$). In the second strategy for obtaining the abasic site product, we incubated the enzyme with OG:P containing DNA for 30 min at room temperature and mixed it with a crystallization solution containing sodium acetate instead of calcium acetate (**Figure 3D**). High concentrations of Na^+ ions reduce MutY performance but do not block the chemical reaction (37). This method excluded calcium before and during crystallization and provided a complex of N146S with an AP site and a small amount of β- and δ-elimination products, that we will refer to as AP-calcium-free (N146S-OG:$AP_{Ca\text{-}free}$). In the final strategy, a crystal structure of the AP product formed *in crystallo* was captured by soaking N146S-OG:P substrate crystals in an EGTA-containing solution for 7 days at room temperature to remove the Ca^{2+} ion inhibitor (**Figure 3E**). This third method ensured that the AP product was generated in the enzyme active site after crystallization. We will refer to this product structure where the AP site was generated by EGTA chelation as AP-calcium-depleted (N146S-OG:$AP_{Ca\text{-}depleted}$). The AP product structures of MutY obtained by these three different strategies revealed an exciting outcome in that only the β anomer of the AP site was observed consistent with retention of stereochemistry. Details of the N146S structures will be further discussed in the following sections.

Intact Purine Coordinates to a Ca^{2+} in the Active Site of N146S

Initial maps for N146S-OG:P revealed several features indicating intriguing structural differences relative to the MutY-DNA structure used for molecular replacement. Strong negative density highlighted the carboxamide side chain of residue 146 in the |Fo|-|Fc| map consistent with replacement with a smaller amino acid. We also observed strong positive density in the position expected for a base within the active site. Accordingly, we rebuilt position 146 with Ser and modeled the N146S-OG:P complex with an intact purine base (**Figure 4A**). Additional positive features remained in the active site, even after building in the purine base and replacing Asn with Ser at position 146. The region once occupied by the amide group of

Asn146 in previous structures (6, 7) contained a new electron density with an anomalous difference peak indicating the presence of a metal ion. We modeled a Ca^{2+} ion in this region due to high concentration of calcium acetate in our crystallization solution. The purine structure represents the first example of cation metal coordination in the active site of *Gs* MutY. We hypothesize that replacement of Asn146 with a smaller serine residue allowed space for the Ca^{2+} ion to coordinate with active site residues, a phosphate of DNA backbone, and the purine base itself in the N146S-OG:P structure.

The Fe-S cluster cofactor in the N-terminal domain of MutY was modeled with two different conformations, with each alternate conformation supported by strong anomalous difference signals for each iron atom in both conformations (**Figure 4B**). Conformation B retains the overall shape of conformation A, but the atoms are translated 1.86 (±0.09) Å in a direction that is nearly perpendicular to the nearby alpha helix comprising residues 145-156. This suggests the possibility of communication with the active site as this helix contributes the residue at position 146 and is capped by the catalytically critical residue Asp 144 (**Figure S2A**). The iron-coordinating cysteine residues (198, 205, 208, and 214) accommodate the movement of the iron-sulfur cluster by adopting corresponding alternate conformations to maintain the interactions with the Fe-S cluster. However, the impact on structure appears highly localized as neighboring residues are satisfactorily modeled with single conformations. The reason why we see alternate conformations while other structures of MutY only include a single conformation for the Fe-S cluster probably relates to the very high 1.54-Å resolution limit obtained for our diffraction data. Indeed, the structure with an enzyme-generated AP site that we refined to the 1.68-Å resolution limit (N146S-OG:$AP_{Ca\ free}$, described below) also features alternate conformations for the Fe-S cluster.

Another unusual structural feature involves the adenine neighboring the purine nucleotide. Adenine-17 which is 5' to the substrate purine at position 18 assumes an unusual *syn* conformation to form a Hoogsteen base pair (bp) with thymine (**Figure S2B**). Notably, recent work has shown that Hoogsteen bps are often present in protein-DNA complexes at "stressed" or distorted sites such as those proximal to lesions, metal ions and nicks (38). Intriguingly, Ca^{2+} coordination in the active site likely leads to a chain of conformational perturbations that emanate from the DNA phosphate backbone to the neighboring adenine nucleotide and the Fe-S cluster.

In the N146S-OG:P structure, the purine nucleotide adopts a conformation that appears incompatible with catalysis. As a consequence of Ca^{2+} ion coordination, N7 of the purine base is 4 Å away from Glu43, significantly farther than 2.8 Å observed in the previously published substrate-enzyme structure (6), and too far for facile protonation of the base in the first step of catalysis (**Figure 4C-F**). Despite the observed activity of N146S *Gs* MutY *in vitro*, the presence of the Ca^{2+} ion during crystallization appears to have stalled the ability of enzyme to protonate N7 of purine by Glu43 needed for catalysis. The lack of engagement of the adenine base with Glu43 was similarly observed in the Lesion Recognition Complex (LRC, PDB ID 1RRQ) that replaced Asp 144 with asparagine to prevent catalysis (D144N), (**Figure 4E**) (39). The non-productive orientation of purine seen in N146S-OG:P is most likely a consequence of coordination of N3 of purine to the Ca^{2+} ion and the absence of the 6-amino group, normally present in

adenine for hydrogen-bonding and positioning with Glu188. Indeed, Glu188 adopts a different rotamer away from the base that is not completely engaged in the LRC structure (39) as well as in the N146S-OG:P structure (**Figure 4F**). The disengaged base position seen in the LRC and the N146S-OG:P structure described here suggests subtle changes in active site residues alter the proper alignment of the base, which is likely a key quality control mechanism by MutY, and is consistent with previous work that showed reduced activity with structural changes in A (35).

The ability of Ca^{2+} ions present during crystallization to stall purine excision suggested that metal cations may generally inhibit MutY glycosylase activity. We tested for metal inhibition under single turnover conditions in the presence of Mg^{2+}, Ca^{2+} and Na^{+} ions (**Figure S1**). Glycosylase assays of WT and N146S *Gs* MutY with OG:A-containing DNA in the presence of Mg^{2+} and Ca^{2+} showed significantly reduced activity at concentrations of either divalent metal above 15 mM. The diminished activity was similar for both WT and N146S *Gs* MutY indicating reduced activity is not specific to mutation of Asn146. Notably, similar concentrations of Na^{+} ions did not prevent product formation by WT MutY or the N146S variant, indicating that the abolished activity with Mg^{2+} and Ca^{2+} is specific to divalent metal ions.

Asp144 Loses its Hydrogen Bond Partner

In the second class of crystal structures containing a transition state analog, N146S-OG:1N, many active site residues assume similar conformations and interactions as seen in previous structures of the enzyme (6, 7)**.** Similar to the TSAC-OG:1N structure, N146S-OG:1N features close approach of the carboxylate group of Asp144 with the positively charged secondary amine of 1N (N1'), explaining the high affinity for 1N containing DNA and indicating stabilization of the transition state is a major contributor to catalysis for both enzymes. Also, highly comparable to the original TSAC structure, N146S-OG:1N harbors a water molecule located between Glu43 and N1' consistent with the proposal that abasic site product formation occurs with activation of the nucleophile by Glu43 and attack from the 5' face of the sugar. These preserved structural features strongly suggest that N146S *Gs* MutY uses a mechanism similar to that of the WT enzyme.

The significant structural differences revealed by comparing the two TSAC structures appear to be localized to the interaction of residue 146 with DNA and Asp144. Because of the different sizes of Asn and Ser, the residue at position 146 is located much farther from Asp144 in N146S-OG:1N. The carboxamide nitrogen of the Asn146 side chain is positioned 2.9 Å away from the carboxylate oxygen of Asp144 in the TSAC-OG:1N structure (**Figure 1B**), while the corresponding distance to the hydroxyl oxygen of Ser146 was measured as 4.7 Å in N146S-OG:1N (**Figure 5A**). Similarly, the closest distance from residue 146 to the 5'-phosphate group of the transition state analog was measured as 4.6 Å in N146S-OG:1N, much further than the 3.0 Å measured for TSAC-OG:1N. In other words, Ser at position 146 is too small and positioned too far away to maintain a hydrogen bonding network analogous to that in the wild-type enzyme with the DNA phosphodiester backbone and Asp144.

Structural insights from both N146S-OG:P and N146S-OG:1N showed loss of hydrogen bond interaction to Asp144 even as this residue maintains stabilizing interactions with the transitions state mimic,

providing a structural basis for the biochemical impact of the asparagine to serine replacement. Indeed, the hydrogen bond interaction of Asn146 with Asp144 seen in structures of wild-type *Gs* MutY may be modulating the pK_a of Asp144, and loss of this hydrogen bond to Asp144 may increase its pK_a in N146S MutY contributing to reduced activity. We performed a pH-dependent kinetics experiment for N146S *Gs* MutY to test for a potential shift in the pK_a of Asp144 due to loss of hydrogen bonding upon replacement of Asn146 with serine. We evaluated the pH dependence of the observed rate of adenine removal (k_{obs}) for WT and N146S *Gs* MutY under single turnover conditions for the pH range of 4.0-10.5 (**Figure S3A**)**.** The pK_a of Asp144 for WT *Ec* MutY has been previously reported as 4.9 from the one-legged curve in which rate decreases with decreasing pH values between 7.5 and 4.0 (23). Both WT and N146S *Gs* MutY have been shown to display a bell-shaped curve where the rate of adenine excision decreases with decreased pH between 7.5 and 4.0 as well as with the increased pH between 8.0 and 10.0 (**Figure S3A**). Additionally, a dip is observed between pH 5.0 and 6.0. A similar pH profile was observed with WT *Ec* MutY using the G:A containing substrate and it was interpreted as presence of three residues affecting the pH profile with pK_as of 4.8, 6.1 and 8.8 (23). The first pK_a of 4.8 overlaps with the pK_a of Asp144 supporting the idea that the pK_a of Asp144 can be obtained between pH 4.0 and 5.5 range. When the pH profiles of WT and N146S variant overlayed, the increase in pK_a of Asp144 is visually apparent in the shift of the curve in the pH range of 4-5.5 (**Figure S3B**). Approximately, a ~0.5-1 pH unit increase was estimated from the curves for the shift in the pK_a of Asp144 in N146S *Gs* MutY by fitting the data in the pH range of 4.0-6.0.

The increased pK_a of Asp144 in N146S *Gs* MutY suggests that the presence of hydrogen bond partner asparagine may contribute to maintaining the deprotonated state of the Asp residue needed for transition state stabilization as positive charge accumulates on C1'. Notably, in *Bacillus circulans* β-xylanase (Bcx) the pK_a of the nucleophilic Glu (Glu78) was shown to be modulated by H-bonding with a Tyr residue (Tyr69) and a nearby Gln residue analogous to the Asp/Asn interaction in MutY (40). In addition, replacement of Glu78 with 4-fluoroglutamic acid or 4,4-difluoroglutamic acid that exhibited reduced pK_as, resulted in increased leaving group ability of the introduced Glu from the covalent enzyme-substrate intermediate (41). In this context, the increase in pK_a of Asp resulting from replacement of Asn with Ser may have altered the participation of Asp144 as a nucleophile in the adenine excision step and also altered its leaving group potential in the hydrolysis of an MutY-DNA acetal intermediate. Hence, a more stable covalent acetal intermediate due to the altered pK_a of Asp144 may be a significant factor of the reduced activity of N146S *Gs* MutY. The sensitivity of the pK_a of Asp144 to the Asn mutation, and dramatic influence of this subtle change on activity is indicative of fine-tuning of electrostatics and H-bonding present in the MutY active site to optimize catalysis.

Abasic Site Product Captured Coordinated to a Calcium in the Active Site of N146S

Increasing the incubation time of N146S with the OG:P substrate, prior to initiation of crystallization with the calcium acetate conditions, provided a structure of N146S *Gs* MutY bound to its AP site product (N146S-OG:$AP_{Ca\text{-}inhibited}$, **Figure 3C**). The formation of the AP site product was immediately clear by inspection of the electron density maps that closely outlined the deoxyribose sugar and the absence of

electron density for the purine base. We observed strong additional density close to the hydroxyl of Ser146 and the carboxylate of Asp144, similar to the situation observed in the N146S-OG:P, and interpreted this as a Ca^{2+} ion with partial occupancy (**Figure 6A&B**). The Ca^{2+} ion is coordinated by Ser146, Asp144 and surrounding DNA phosphate groups. The concentration of negatively charged groups in this region explains why a metal ion would be attracted to this site. The Ca^{2+} ion refined best with partial occupancy meaning it is not held as tightly as seen for N146S-OG:P, a situation explained since now the purine base is not covalently attached and no longer contributes to the coordination sphere. Indeed, our understanding of the inhibitory impact of divalent metal ions on the reaction and the absence of electron density for the purine base strongly indicates that substrate converted to the AP product *before* the reaction was mixed with the calcium-containing crystallization solution.

The β-anomer AP site product fit to the electron density maps calculated to 2.4 Å for N146S-OG:$AP_{Ca\text{-}inhibition}$, with minor residual positive and negative features (**Figure 6A**). The potential for the presence of α anomer of the AP site was also tested based on AP site product structures reported with MBD4, UDG, and TDG that showed formation of a single α or mixture of α/β anomer AP site product (42–44). The maps calculated for the N146S-OG:$AP_{Ca\text{-}inhibition}$ structure rebuilt with α anomer AP site featured a poor fit for the sugar group and a strong positive signal in the space where a β anomer hydroxyl group would occupy (**Figure 6B**). The result of this anomer test strongly indicates that the α anomer is incompatible with our X-ray diffraction data. We further analyzed the AP site stereochemistry with the higher resolution data measured for Ca-free AP product structure as described in the following section, ultimately reaching the same conclusion that the enzyme-generated AP product found at the active site of MutY is a closed-ring β anomer consistent with retention of stereochemistry.

Abasic Site Product Structures Inform the Adenine Excision Mechanism of MutY that Proceeds with Retention of Stereochemistry

We next evaluated Ca^{2+} free strategies to trap the AP site product. We crystallized the N146S with OG:P containing DNA using a previously reported crystallization condition containing sodium acetate (25) in place of calcium acetate with the expectation that glycosylase activity would be retained during and possibly after crystallization. The crystal obtained in this calcium free condition afforded the highest resolution (1.68 Å) view of the enzyme-catalyzed ring-closed AP product structure (**Figure 6C**). Density for the calcium ion in the AP-Ca-inhibited structure had prevented a clear view of the AP site, but such is not the case for the N146S AP-Ca-free structure. We see an unobstructed view of the AP site with clear indication of the beta anomer. Given the importance of this stereochemical configuration for the MutY mechanism, we wanted to be extra careful to not overlook alternate interpretations and therefore tested both the beta anomer and alpha anomer of the AP site in several sugar puckers. In each case, regardless of which sugar pucker was analyzed, the alpha anomer refined with an unrealistically high temperature factor for the hydroxyl group, fit poorly to the electron density, and left a prominent positive feature in the $|F_o| - |F_c|$ difference map (**Figure S4A-D**). Hence, we could confidently eliminate this configuration and conclude that the MutY-generated AP site is the beta anomer. Assignment of the sugar pucker for the beta

anomer was less clearcut since C3'-exo, C2'-endo and C1'-exo each fit the electron density (**Figure S4E-H**). However, refinement with weaker torsion angle restraints always resulted in the structure relaxing to the C3' exo sugar pucker. Although C3'-exo is considered unstable relative to C3'-endo and C2'-endo sugar puckers in normal DNA, interaction with the active site and absence of the base moiety probably create a different energy landscape with respect to pseudorotation. Indeed, the computational KIE study for MutY indicated C3'-exo pucker is the most stable conformation observed for the transition state and oxacarbenium ion intermediate in an S_N1-like mechanism (8). In addition, the N146S-OG:1N transition state structure suggested the mechanism remains unchanged with replacement of Asn146 with serine, hence we selected β anomer product formation with 3-exo sugar pucker by implication from the mechanism, KIE studies and structural insights.

Additional interesting features were observed in the N146S-OG:$AP_{Ca\text{-}free}$ structure after the analysis of the active site pocket. These included alternate conformations for the Fe-S cluster (**Figure S5A**) as previously noted above and further discussed in a separate section below. Electron density peaks nearby the phosphate groups connecting the AP site to its nucleotide neighbors in maps calculated for N146S-OG:$AP_{Ca\text{-}free}$ indicated strand cleavage consistent with minor (~20%) side products resulting from β and δ elimination. Accordingly, we modeled alternate conformations for the free 3' phosphate (3'P) and 5' phosphate (5'P) groups and adjusted the occupancy of the AP site (**Figure 6D and S5B**). We looked for but could not find unambiguous electron density defining the nucleotide remanent expected after β-elimination and before δ-elimination. This species may be relatively unstable or may assume multiple conformations. Indeed, a recent extensive study of products derived from chemical reactions involving the AP abasic site in DNA established that strand breaks and several remanent nucleotide species are formed with heat or long incubation times (45). Notably, low levels of "adventitious" β-elimination at the AP site has also been previously seen in *Ec* MutY (46, 47).

A glutamine residue, Gln48, intercalates with the DNA to fill a void created when adenine is extruded into the active site of MutY. Electron density maps indicated this residue adopts alternate conformations in the structure of N146S-OG:$AP_{Ca\text{-}free}$. Conformer A is commonly observed in structures of MutY making aromatic stacking interactions with bases of the DNA and hydrogen bonding with the phosphate group connecting the substrate nucleotide (or transition state analog) to its 3'-nucleotide neighbor dG-19 (6, 7, 48). Conformer B of Gln48 retains its interaction with the alternate conformer B of the free 5' phosphate group of dG-19 generated by beta elimination (**Figure 6D and S5B**). This conformer B of Gln48 has also been previously observed in structures of *Gs* MutY, in complex with the reduced AP product (PDB ID: 1VRL) (39) and in complex with anti-substrate (PDB ID: 4YOQ) (25). Each of these previously described structures features an "exo" site engaged with a chemical group, either the reduced AP product or the cytosine of the OG:C anti-substrate. In these structures, Gln48 adopts a different conformation to maintain its interaction with the 5' phosphate backbone even as it is displaced to accommodate interactions with the "exo" site. Our structure does not show any molecule present in the

"exo" site; however, the alternate conformer B of Gln48 fits in the same conformation to maintain similar interactions with the 5' phosphate backbone resulting from β-elimination.

Having successfully replaced Ca^{2+} with Na^{+} in crystallization conditions, we next aimed to initiate the excision of purine *in crystallo* by removing the Ca^{2+} in N146S-OG:P crystals and trapping the resulting product by freezing. For this strategy, we incubated an N146S-OG:P crystal in a solution containing EGTA that chelates Ca^{2+} ions. Preliminary trials showed that small soaking volumes and short incubation times (5 min to 2 hr) with either EDTA or EGTA were insufficient to completely remove calcium ions from crystals as evidenced by electron density maps. The crystal that provided the N146S-OG:$AP_{Ca\text{-}depleted}$ structure was serially washed in small volumes of the EGTA solution, and then incubated in a 2 mL reservoir of the EGTA solution for one week to allow sufficient time for the Ca^{2+} removal and product accumulation. The advantage of this strategy is that release of DNA, an outcome that is already unlikely because of very high affinity of MutY for its product, but which could promote anomerization, is made highly improbable in the crystalline state. The Ca-depletion strategy succeeded as evidenced by no indication of Ca^{2+} ions either at the active site or at the metal ion-binding site involving Ser118 and a phosphate of the DNA seen in previous structures. Although EGTA chelates Fe ions in solution, the electron density maps showed no loss of Fe-S cluster after chelator treatment that depleted calcium. Removal of Ca^{2+} initiated the MutY reaction in the crystalline state as evidenced by clear density outlining the enzyme-generated AP product as its closed-ring beta anomer and an absence of density for the base moiety in the structure for N146S-OG:$AP_{Ca\text{-}depleted}$ (**Figure 6E**). As previously described for the N146S-OG:$AP_{Ca\text{-}free}$ structure, extra density by the phosphate linking the AP site in N146S-OG:$AP_{Ca\text{-}depleted}$ with its 3'-nucleotide neighbor indicated strand cleavage for the phosphodiester bond and minor accumulation (~40%) of a side product through β-elimination. We made several attempts to build the nucleotide remanent, ultimately concluding that the positive features in electron density maps could not unambiguously define a single conformation, probably due to the existence of multiple conformers and instability with respect to subsequent delta elimination. These exciting results demonstrate MutY catalyzes base excision from a substrate mispair within DNA in crystals, mitigating the product racemization caveat, and therefore establishing the stereochemistry of the hydrolysis product providing important implications for the retaining MutY mechanism.

Conformations of Iron-Sulfur Cluster in N146S Structures

Among the five structures of the N146S variant we observe a variance in conformational flexibility for the Fe-S cluster. In the higher resolution structures, N146S-OG:P and N146S-OG:$AP_{Ca\text{-}free}$, two conformations for the Fe-S cluster were supported by strong features in the electron density maps including the map calculated with anomalous difference signals. On the other hand, the N146S-OG:1N structure harbors a single conformation for the Fe-S cluster, corresponding to conformer A in the structures with alternate conformations, and evidenced by the anomalous difference map clearly highlighting Fe and S atoms (**Figure 5B**). While we can explain lack of alternate Fe-S conformations for the Ca-depleted and Ca-inhibited AP structures based on relatively lower resolution, the transition state structure was refined to the 1.96-Å resolution limit with 0.33-Å coordinate error, sufficient to detect a nearly 2-Å shift in Fe-S position if

present. The presence of alternate Fe-S conformations in some but not other high-resolution structures for the N146S variant suggests that a mechanism may exist to communicate changes in the active site to influence Fe-S cluster positional flexibility. We speculate that the presence of Ca^{2+} metal ion coordination in the active site of N146S-OG:P led to subtle conformational adjustments and changes in the electrostatic field that were transmitted via the DNA phosphate backbone and involving the alpha helix with residues Ser146 and Arg149, finally impinging on the Fe-S cluster via Cys198 (**Figure S2C**). Similarly, distortions in the DNA backbone resulting from β elimination could activate this mechanism to realize alternate positions for Fe-S in the N146S-OG:$AP_{Ca\text{-}free}$ structure. In support of these ideas, previous work has shown that the Fe-S cluster is more easily oxidized when MutY is bound to DNA indicating that alterations resulting from DNA binding impact the Fe-S cluster environment and properties (49). The mechanism for communication seems to work in both directions as different oxidation states of the cluster appear to be transmitted to the active site and influence adenine excision (50).

Implications for the Adenine Excision Mechanism

The snapshots of N146S *Gs* MutY described in previous sections provided us a nearly complete structural movie of the purine excision mechanism (**Movie S1**). We first captured the purine intact in the active site before it was excised by the enzyme, albeit in an unproductive conformation, too far away for protonation by Glu43 due to calcium coordination. We believe removal of the calcium ion allows the base to assume the productive conformation for the protonation step of the mechanism. The transition state structure N146S-OG:1N showed a water molecule between Glu43 and N1 as previously seen in the TSAC-OG:1N, suggesting the base excision mechanism occurs through a similar double displacement mechanism for the Asn-to-Ser variant. The stereochemical analysis of the product of the MutY-catalyzed methanolysis reaction had previously indicated formation of the AP product in the hydrolysis reaction proceeds with retention of stereochemistry (7). Our enzymatically formed ring-closed AP site product structures with N146S provide new direct evidence for the β-anomer formation with retention of stereochemical configuration, necessitating that the water nucleophile approaches from the same side as leaving group departure, and validating inferences from the methanolysis experiment. The AP product structures lack clear density for the cleaved base in the active site, consistent with diffusion of the leaving group away from the sugar to avoid steric clashes as the water nucleophile moves into position close to Glu43. During the intervening time, the highly unstable oxacarbenium ion transition state intermediate is stabilized by strong interaction with Asp144, probably by forming a transient covalent intermediate.

Enzymatically generated AP sites have been observed in structures of other DNA glycosylases, and comparisons provide insight into mechanism and evolution of this important family. Previously, the wtUDG-product complex containing a cleaved uracil base nearby the 5' face of the sugar featured the α anomer AP site product (43). However, L272A UDG was captured with the β anomer AP product and also missing the cleaved uracil in the active site. The different outcomes for UDG and its L272A variant were rationalized by DNA binding kinetics which make it more likely for L272A UDG to release the product and provide an opportunity for anomerization of AP site product (43). Similarly, TDG was found in complex with

α-anomer AP site product alongside an acetate ion in the active site (44). With removal of acetate from crystallization conditions, TDG was trapped with a mixture of α and β anomers (51), suggesting either anomerization of the AP product or formation of AP product through a stereochemically ambivalent S_N1 mechanism where water can attack from either side of the sugar.

By contrast to these examples with mixed outcomes, our product structures consistently showed a single β anomer despite applying three different strategies for its capture. Furthermore, the high affinity of MutY to its product makes it highly probable that the product formed was retained in the active site without DNA rebinding events. Opportunity for anomer reorganization was especially unlikely when we precrystallized the MutY-OG:P DNA complex and initiated enzyme-catalyzed purine excision *in crystallo* by calcium ion depletion (with EGTA). Precedent for capture of enzyme-generated AP site in a pure stereochemical configuration comes from a recent MBD4 structure which showed a single α-anomer AP site with no interference by cleaved base or crystallization compounds (42).

These structures indicate the formation of anomers appears to depend highly on the active site structure. Indeed, while UDG and MBD4 each harbor an Asp residue that coordinates the water nucleophile for α-anomer formation, TDG is missing a comparable carboxylate-bearing residue and the resulting lack of direction probably contributes to the observed mixed stereochemistry. MutY harbors an Asp for transition state stabilization and a Glu that coordinates and activates the water nucleophile for attack, a constellation of chemical groups that ensures a single beta anomer outcome as observed in our new structures of N146S MutY. Our findings are consistent with the idea that the Glu residue in MutY is not only important for adenine protonation but also for activating and positioning the water nucleophile, and thereby directing stereochemistry of the AP site product.

Significance of the Mechanistic Findings in Cancer

The cancer association of inherited variants of MUTYH highlights the importance of understanding how MutY functions to recognize its substrate and excise its target base. The biochemical and structural study of the MAP associated Asn-to-Ser variant in bacterial MutY revealed the significance of the asparagine residue in adenine excision. Our findings suggested that this asparagine plays an active role and its replacement with serine, as found in MAP, significantly impairs catalysis due to disruption of the hydrogen bond network with the catalytic aspartate and DNA. The human MUTYH active site harbors a similar structure to the bacterial homologs, each containing the highly conserved catalytic Glu and Asp residues with their hydrogen bonding partners, Tyr and Asn (52). It is therefore reasonable to infer the MUTYH MAP variant N238S may also have altered catalytic activity due to severed hydrogen bond interactions, thus explaining accumulation of OG:A mispairs and early onset of cancer. Furthermore, the active site structure of N146S-OG:P with a Ca^{2+} ion coordinating to an intact purine base suggests that excision of the target base may be impaired by invasion of transition metals. In a medical context, the inhibitory effect of metal coordination in the additional space made available by the N238S mutation may additionally contribute to underperformance of this MAP variant.

Conclusion

Our extensive investigation revealed the biochemical and structural significance of the Asn residue immediately adjacent to a catalytic Asp residue in the MutY active site. Structure determination with a substrate and a transition state analog showed that the Asn residue is critical for establishing a hydrogen-bonding network involving catalytic residues and the DNA. Activity performance and pH profile alterations highlight the role of the Asn in fine-tuning the pK_a and nucleophilic character of the catalytic Asp. Interestingly, despite the excision ability of the Asn-to-Ser variant, we captured N146S *Gs* MutY with OG:P containing DNA with calcium ion coordination in the active site apparently preventing base removal. Further crystallization studies revealed the removal of this Ca^{2+} ion from the active site can initiate adenine excision, providing a method to trap different steps of the mechanism in a crystalline state. Indeed, when Ca^{2+} ion was removed from the active site using EGTA or by excluding divalent metal ions from crystallization solutions, an enzyme-catalyzed AP product structure in complex with the MutY N146S variant was obtained. Furthermore, crystallization of N146S with OG:P under Ca-free, Ca-inhibited and Ca-depleted conditions each revealed exclusively the β anomer of the AP product, thus extending current evidence for a retaining MutY mechanism. In conclusion, the structural snapshots of N146S *Gs* MutY have created a structural movie showing several steps of the purine excision mechanism, including base mis-engagement, transition state stabilizing interactions, and stereochemistry of the AP product formation in the active site, and provides further evidence for the double displacement mechanism of MutY.

ACCESSION NUMBERS

Structures were deposited to the Protein Data Bank with PDB ID: 8DVP, 8DW7, 8DW0, 8DVY, 8DW4.

SUPPLEMENTARY DATA

Supplementary Data are available at NAR online.

FUNDING

This work was funded by the National Science Foundation [awards 1905249 to M.P.H.; awards 1905304 to S.S.D.]. C.H.T.A was supported by a UCMEXUS-CONACYT Postdoctoral Fellowship. Beamline 8.3.1 at the Advanced Light Source is operated by the University of California at San Francisco with generous grants from the National Institutes of Health (R01 GM124149 for technology development and P30 GM124169 for beamline operations), and the Integrated Diffraction Analysis Technologies program of the US Department of Energy Office of Biological and Environmental Research. The Pilatus detector at Beamline 5.0.1. was funded under NIH grant S10OD021832. The Advanced Light Source (Berkeley, CA) is a national user facility operated by Lawrence Berkeley National Laboratory on behalf of the US Department of Energy under contract number DE-AC02-05CH11231, Office of Basic Energy Sciences.

CONFLICT OF INTEREST

Authors declare no conflict of interest.

ACKNOWLEDGEMENT

We thank ALS beamline staff George Meigs, Kevin Royal and Marc Allaire for their assistance in data collection. We also thank the Beal and Fisher Laboratories at UC Davis for their assistance in providing instruments and tools.

REFERENCES

1. Michaels,M.L. and Miller,J.H. (1992) The GO system protects organisms from the mutagenic effect of the spontaneous lesion 8-hydroxyguanine (7, 8-dihydro-8-oxoguanine). *J. Bacteriol.*, **174**, 6321–6325.
2. Brieba,L.G., Eichman,B.F., Kokoska,R.J., Doublié,S., Kunkel,T.A. and Ellenberger,T. (2004) Structural basis for the dual coding potential of 8-oxoguanosine by a high-fidelity DNA polymerase. *EMBO J.*, **23**, 3452–3461.
3. Al-Tassan,N., Chmiel,N.H., Maynard,J., Fleming,N., Livingston,A.L., Williams,G.T., Hodges,A.K., Davies,D.R., David,S.S., Sampson,J.R., *et al.* (2002) Inherited variants of MYH associated with somatic G:C→T:A mutations in colorectal tumors. *Nat. Genet.*, **30**, 227–232.
4. Raetz,A.G. and David,S.S. (2019) When you're strange: Unusual features of the MUTYH glycosylase and implications in cancer. *DNA Repair (Amst).*, **80**, 16–25.
5. McCann,J.A.B. and Berti,P.J. (2003) Adenine Release Is Fast in MutY-catalyzed Hydrolysis of G:A and 8-Oxo-G:A DNA Mismatches*. *J. Biol. Chem.*, **278**, 29587–29592.
6. Lee,S. and Verdine,G.L. (2009) Atomic substitution reveals the structural basis for substrate adenine recognition and removal by adenine DNA glycosylase. *Proc. Natl. Acad. Sci.*, **106**, 18497–18502.
7. Woods,R.D., O'Shea,V.L., Chu,A., Cao,S., Richards,J.L., Horvath,M.P. and David,S.S. (2016) Structure and stereochemistry of the base excision repair glycosylase MutY reveal a mechanism similar to retaining glycosidases. *Nucleic Acids Res.*, **44**, 801–810.
8. Berti,P.J. and McCann,J.A.B. (2006) Toward a detailed understanding of base excision repair enzymes: transition state and mechanistic analyses of N-glycoside hydrolysis and N-glycoside transfer. *Chem. Rev.*, **106**, 506–555.
9. Guan,Y., Manuel,R.C., Arvai,A.S., Parikh,S.S., Mol,C.D., Miller,J.H., Lloyd,R.S. and Tainer,J.A. (1998) MutY catalytic core, mutant and bound adenine structures define specificity for DNA repair enzyme superfamily. *Nat. Struct. Biol.*, **5**, 1058–1064.
10. Gloster,T.M. and Davies,G.J. (2010) Glycosidase inhibition: assessing mimicry of the transition state. *Org. Biomol. Chem.*, **8**, 305–320.
11. Vocadlo,D.J., Davies,G.J., Laine,R. and Withers,S.G. (2001) Catalysis by hen egg-white lysozyme

proceeds via a covalent intermediate. *Nature*, **412**, 835–838.
12. Zechel,D.L. and Withers,S.G. (2001) Dissection of nucleophilic and acid–base catalysis in glycosidases. *Curr. Opin. Chem. Biol.*, **5**, 643–649.
13. Dallosso,A.R., Dolwani,S., Jones,N., Jones,S., Colley,J., Maynard,J., Idziaszczyk,S., Humphreys,V., Arnold,J. and Donaldson,A. (2008) Inherited predisposition to colorectal adenomas caused by multiple rare alleles of MUTYH but not OGG1, NUDT1, NTH1 or NEIL 1, 2 or 3. *Gut*, **57**, 1252–1255.
14. Raetz,A.G., Xie,Y., Kundu,S., Brinkmeyer,M.K., Chang,C. and David,S.S. (2012) Cancer-associated variants and a common polymorphism of MUTYH exhibit reduced repair of oxidative DNA damage using a GFP-based assay in mammalian cells . *Carcinogenesis*, **33**, 2301–2309.
15. Chu,A.M., Fettinger,J.C. and David,S.S. (2011) Profiling base excision repair glycosylases with synthesized transition state analogs. *Bioorg. Med. Chem. Lett.*, **21**, 4969–4972.
16. Aslanidis,C. and De Jong,P.J. (1990) Ligation-independent cloning of PCR products (LIC-PCR). *Nucleic Acids Res.*, **18**, 6069–6074.
17. Li,C., Wen,A., Shen,B., Lu,J., Huang,Y. and Chang,Y. (2011) FastCloning: a highly simplified, purification-free, sequence-and ligation-independent PCR cloning method. *BMC Biotechnol.*, **11**, 1–10.
18. Nakamura,M., Saeki,K. and Takahashi,Y. (1999) Hyperproduction of Recombinant Ferredoxins in Escherichia coli by Coexpression of the ORF1-ORF2-iscS-iscU-iscA-hscB-hscA-fdx-ORF3 Gene Cluster1. *J. Biochem.*, **126**, 10–18.
19. Fromme,J.C. and Verdine,G.L. (2002) Structural insights into lesion recognition and repair by the bacterial 8-oxoguanine DNA glycosylase MutM. *Nat. Struct. Biol.*, **9**, 544–552.
20. Nuñez,N.N., Majumdar,C., Lay,K.T. and David,S.S. (2018) Chapter Two - Fe–S Clusters and MutY Base Excision Repair Glycosylases: Purification, Kinetics, and DNA Affinity Measurements. In David,S.S.B.T.-M. in E. (ed), *Fe-S Cluster Enzymes Part B*. Academic Press, Vol. 599, pp. 21–68.
21. Porello,S.L., Leyes,A.E. and David,S.S. (1998) Single-Turnover and Pre-Steady-State Kinetics of the Reaction of the Adenine Glycosylase MutY with Mismatch-Containing DNA Substrates. *Biochemistry*, **37**, 14756–14764.
22. Richards,J.L. (2008) Recognition and Repair of DNA Damage by Bacterial Adenine Glycosylases.
23. Brinkmeyer,M.K., Pope,M.A. and David,S.S. (2012) Catalytic Contributions of Key Residues in the Adenine Glycosylase MutY Revealed by pH-dependent Kinetics and Cellular Repair Assays. *Chem. Biol.*, **19**, 276–286.
24. Porello,S.L., Williams,S.D., Kuhn,H., Michaels,M.L. and David,S.S. (1996) Specific Recognition of Substrate Analogs by the DNA Mismatch Repair Enzyme MutY. *J. Am. Chem. Soc.*, **118**, 10684–10692.
25. Wang,L., Lee,S.-J. and Verdine,G.L. (2015) Structural Basis for Avoidance of Promutagenic DNA Repair by MutY Adenine DNA Glycosylase*. *J. Biol. Chem.*, **290**, 17096–17105.

26. Bergfors,T. (2003) Seeds to crystals. *J. Struct. Biol.*, **142**, 66–76.
27. Kabsch,W. (2010) Xds. *Acta Crystallogr. Sect. D Biol. Crystallogr.*, **66**, 125–132.
28. Adams,P.D., Afonine,P. V, Bunkóczi,G., Chen,V.B., Davis,I.W., Echols,N., Headd,J.J., Hung,L.-W., Kapral,G.J. and Grosse-Kunstleve,R.W. (2010) PHENIX: a comprehensive Python-based system for macromolecular structure solution. *Acta Crystallogr. Sect. D Biol. Crystallogr.*, **66**, 213–221.
29. Emsley,P., Lohkamp,B., Scott,W.G. and Cowtan,K. (2010) Features and development of Coot. *Acta Crystallogr. Sect. D Biol. Crystallogr.*, **66**, 486–501.
30. Headd,J.J., Echols,N., Afonine,P. V, Grosse-Kunstleve,R.W., Chen,V.B., Moriarty,N.W., Richardson,D.C., Richardson,J.S. and Adams,P.D. (2012) Use of knowledge-based restraints in phenix. refine to improve macromolecular refinement at low resolution. *Acta Crystallogr. Sect. D Biol. Crystallogr.*, **68**, 381–390.
31. Pettersen,E.F., Goddard,T.D., Huang,C.C., Couch,G.S., Greenblatt,D.M., Meng,E.C. and Ferrin,T.E. (2004) UCSF Chimera—a visualization system for exploratory research and analysis. *J. Comput. Chem.*, **25**, 1605–1612.
32. Pettersen,E.F., Goddard,T.D., Huang,C.C., Meng,E.C., Couch,G.S., Croll,T.I., Morris,J.H. and Ferrin,T.E. (2021) UCSF ChimeraX: Structure visualization for researchers, educators, and developers. *Protein Sci.*, **30**, 70–82.
33. Chmiel,N.H., Golinelli,M.-P., Francis,A.W. and David,S.S. (2001) Efficient recognition of substrates and substrate analogs by the adenine glycosylase MutY requires the C-terminal domain. *Nucleic Acids Res.*, **29**, 553–564.
34. Manlove,A.H., McKibbin,P.L., Doyle,E.L., Majumdar,C., Hamm,M.L. and David,S.S. (2017) Structure–Activity Relationships Reveal Key Features of 8-Oxoguanine: A Mismatch Detection by the MutY Glycosylase. *ACS Chem. Biol.*, **12**, 2335–2344.
35. Majumdar,C., McKibbin,P.L., Krajewski,A.E., Manlove,A.H., Lee,J.K. and David,S.S. (2020) Unique Hydrogen Bonding of Adenine with the Oxidatively Damaged Base 8-Oxoguanine Enables Specific Recognition and Repair by DNA Glycosylase MutY. *J. Am. Chem. Soc.*, **142**, 20340–20350.
36. Schramm,V.L. (2011) Enzymatic transition states, transition-state analogs, dynamics, thermodynamics, and lifetimes. *Annu. Rev. Biochem.*, **80**, 703.
37. Livingston,A.L., Kundu,S., Henderson Pozzi,M., Anderson,D.W. and David,S.S. (2005) Insight into the Roles of Tyrosine 82 and Glycine 253 in the Escherichia coli Adenine Glycosylase MutY. *Biochemistry*, **44**, 14179–14190.
38. Shi,H., Kimsey,I.J., Gu,S., Liu,H.-F., Pham,U., Schumacher,M.A. and Al-Hashimi,H.M. (2021) Revealing A-T and G-C Hoogsteen base pairs in stressed protein-bound duplex DNA. *Nucleic Acids Res.*, **49**, 12540–12555.
39. Fromme,J.C., Banerjee,A., Huang,S.J. and Verdine,G.L. (2004) Structural basis for removal of adenine mispaired with 8-oxoguanine by MutY adenine DNA glycosylase. *Nature*, **427**, 652–656.
40. Joshi,M.D., Sidhu,G., Nielsen,J.E., Brayer,G.D., Withers,S.G. and McIntosh,L.P. (2001) Dissecting

the electrostatic interactions and pH-dependent activity of a family 11 glycosidase. *Biochemistry*, **40**, 10115–10139.

41. Kötzler,M.P., Robinson,K., Chen,H.-M., Okon,M., McIntosh,L.P. and Withers,S.G. (2018) Modulating the nucleophile of a glycoside hydrolase through site-specific incorporation of fluoroglutamic acids. *J. Am. Chem. Soc.*, **140**, 8268–8276.
42. Pidugu,L.S., Bright,H., Lin,W.-J., Majumdar,C., Van Ostrand,R.P., David,S.S., Pozharski,E. and Drohat,A.C. (2021) Structural Insights into the Mechanism of Base Excision by MBD4. *J. Mol. Biol.*, **433**, 167097.
43. Parikh,S.S., Mol,C.D., Slupphaug,G., Bharati,S., Krokan,H.E. and Tainer,J.A. (1998) Base excision repair initiation revealed by crystal structures and binding kinetics of human uracil-DNA glycosylase with DNA. *EMBO J.*, **17**, 5214–5226.
44. Malik,S.S., Coey,C.T., Varney,K.M., Pozharski,E. and Drohat,A.C. (2015) Thymine DNA glycosylase exhibits negligible affinity for nucleobases that it removes from DNA. *Nucleic Acids Res.*, **43**, 9541–9552.
45. Haldar,T., Jha,J.S., Yang,Z., Nel,C., Housh,K., Cassidy,O.J. and Gates,K.S. (2022) Unexpected complexity in the products arising from NaOH-, heat-, amine-, and glycosylase-induced strand cleavage at an abasic site in DNA. *Chem. Res. Toxicol.*, **35**, 218–232.
46. Tsai-Wu,J.J., Liu,H.F. and Lu,A.L. (1992) Escherichia coli MutY protein has both N-glycosylase and apurinic/apyrimidinic endonuclease activities on A.C and A.G mispairs. *Proc. Natl. Acad. Sci.*, **89**, 8779–8783.
47. Williams,S.D. and David,S.S. (1998) Evidence that MutY is a monofunctional glycosylase capable of forming a covalent Schiff base intermediate with substrate DNA. *Nucleic Acids Res.*, **26**, 5123–5133.
48. Russelburg,L.P., O'Shea Murray,V.L., Demir,M., Knutsen,K.R., Sehgal,S.L., Cao,S., David,S.S. and Horvath,M.P. (2020) Structural Basis for Finding OG Lesions and Avoiding Undamaged G by the DNA Glycosylase MutY. *ACS Chem. Biol.*, **15**, 93–102.
49. Tse,E.C.M., Zwang,T.J. and Barton,J.K. (2017) The Oxidation State of [4Fe4S] Clusters Modulates the DNA-Binding Affinity of DNA Repair Proteins. *J. Am. Chem. Soc.*, **139**, 12784–12792.
50. Teo,R.D., Du,X., Vera,H.L.T., Migliore,A. and Beratan,D.N. (2021) Correlation between Charge Transport and Base Excision Repair in the MutY–DNA Glycosylase. *J. Phys. Chem. B*, **125**, 17–23.
51. Coey,C.T., Malik,S.S., Pidugu,L.S., Varney,K.M., Pozharski,E. and Drohat,A.C. (2016) Structural basis of damage recognition by thymine DNA glycosylase: Key roles for N-terminal residues. *Nucleic Acids Res.*, **44**, 10248–10258.
52. Luncsford,P.J., Chang,D.-Y., Shi,G., Bernstein,J., Madabushi,A., Patterson,D.N., Lu,A.-L. and Toth,E.A. (2010) A Structural Hinge in Eukaryotic MutY Homologues Mediates Catalytic Activity and Rad9–Rad1–Hus1 Checkpoint Complex Interactions. *J. Mol. Biol.*, **403**, 351–370.
53. Chepanoske,C. Lou, Porello,S.L., Fujiwara,T., Sugiyama,H. and David,S.S. (1999) Substrate

recognition by Escherichia coli MutY using substrate analogs. *Nucleic Acids Res.*, **27**, 3197–3204.
54. Chepanoske,C. Lou, Lukianova,O.A., Lombard,M., Golinelli-Cohen,M.-P. and David,S.S. (2004) A Residue in MutY Important for Catalysis Identified by Photocross-Linking and Mass Spectrometry. *Biochemistry*, **43**, 651–662.

TABLES, FIGURES and LEGENDS

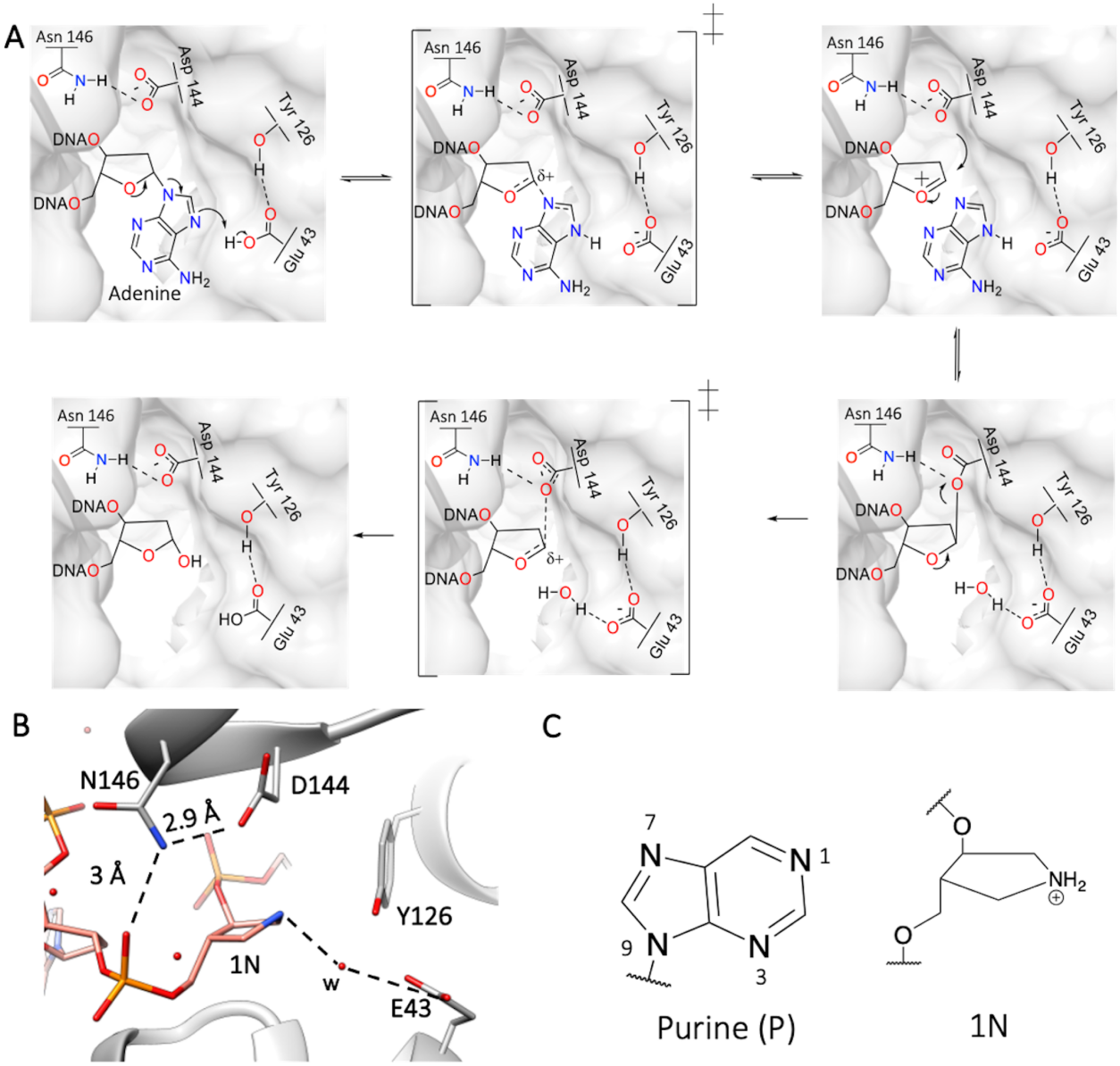

Figure 1 Active site structure and mechanism of MutY (A) Retaining mechanism of adenine excision by DNA glycosylase MutY is an S_N1-like mechanism with formation of a covalent MutY-DNA intermediate (7). (B) The hydrogen bond network between the nucleotide and active site residues shows the interaction between Asn146 and Asp144 (TSAC-OG:1N, PDB ID 6U7T) (7). (C) The structure of substrate purine (P) and pyrrolidine transition state analog (1N) used in this work.

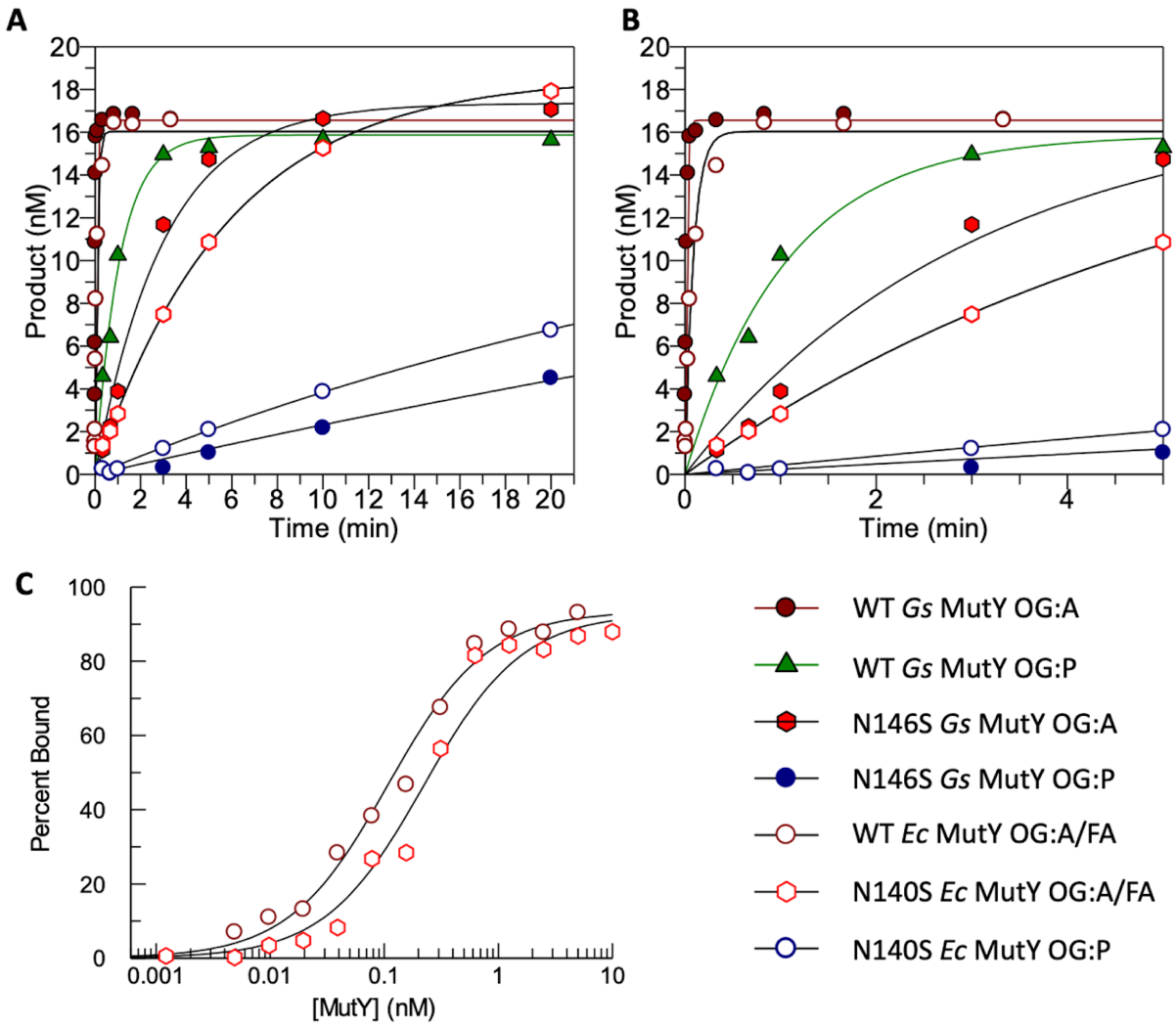

Figure 2 Glycosylase activity and substrate affinity of Asn-to-Ser MutY variants. (A) Representative plots of a single trial used to determine the adenine excision rate, k_2, of each variant with OG:A or OG:P substrates using enzyme concentrations of 120 nM, 100 nM, 40 and 100 nM for WT *Gs,* N146S *Gs*, WT *Ec* and N140S *Gs* MutY, respectively. (B) A zoomed in view of Panel A with time shown up to 5 min. (C) The representative plots of a single trial used to determine the dissociation constant, K_D, of WT[14] and N140S *Ec* MutY with OG:FA containing DNA substrate at 25 °C. The K_D values for WT and N140S *Ec* MutY were representing an average of at least three trials were 0.12±0.02 (53) and 0.14±0.03, respectively.

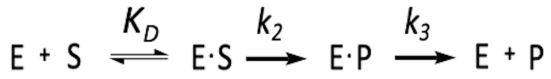

Scheme 1 Minimal Kinetic Scheme of Glycosylase Activity

Table 1: Kinetic parameters of *Gs* and *Ec* MutY variants with OG:A and OG:P containing DNA duplex[a]

MutY	T (°C)	k_3 (min^{-1}) OG:A	k_2 (min^{-1}) OG:A	k_2 (min^{-1}) OG:P
WT *Gs*	60	0.035±0.004[b]	54±4[c]	1.1±0.1
N146S *Gs*	60	0.013±0.004	0.3±0.1	0.012±0.002
WT *Ec*	37	0.004±0.002[d]	12±1[e]	5±1[d]
N140S *Ec*	37	0.005±0.003	0.17±0.01	0.024±0.002

[a] Kinetic parameters k_2 and k_3 were measured using glycosylase assay at 37 and 60 Cº with 20 nM radiolabeled DNA and 30 mM NaCl. Detailed protocol including protein concentrations can be found in Methods and Material section. The dissociation constant K_D was measured using EMSA at 25 Cº with 5 pM radiolabeled DNA and 100 mM NaCl. The kinetic and binding parameters are reported as averages and standard deviations of at least three trials. Due to the absence of biphasic ("burst") kinetics with N146S *Gs* and N140S *Ec* MutY with OG:P containing DNA, the k_3 values could not be determined in these assays. The k_3 value for WT Ec MutY with OG:P was previously measured as 0.003±0.001 min^{-1} (33). [b]Value previously reported (22). [c]Value previously reported (7) [d]Value previously reported (33). [e]Value previously reported (54)

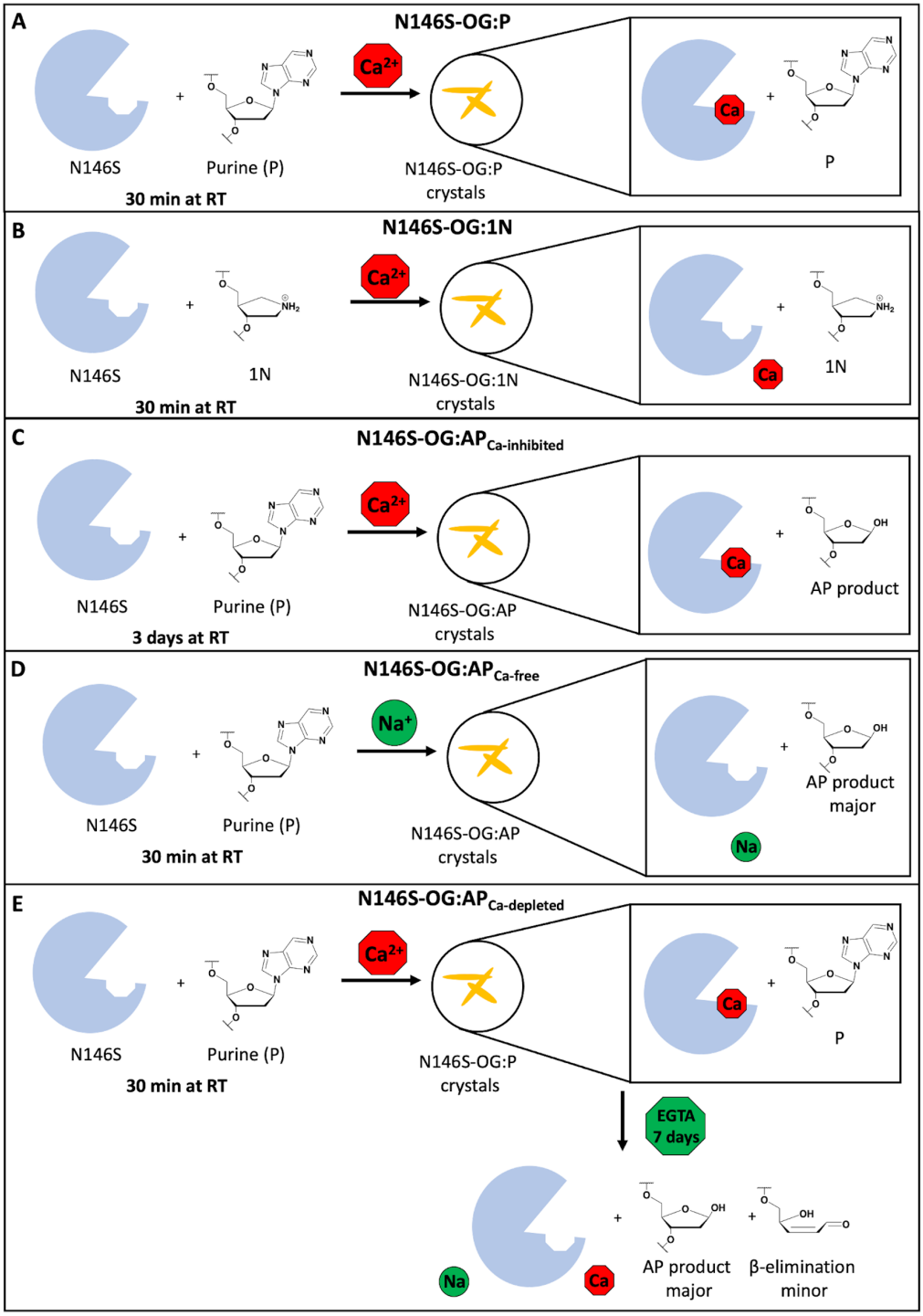

Figure 3 Crystallization Strategies. (A) N146S-OG:P, (B) N146S-OG:1N, (C) and N146S-OG:AP$_{Ca\text{-}inhibited}$ crystallized with calcium containing crystallization solution with their corresponding incubation time and temperature. (D) Crystallization conditions containing sodium instead of calcium for obtaining N146S-OG:AP$_{Ca\text{-}free}$. (E) The N146S-OG:P crystals soaked in EGTA containing solution for 7 days to remove calcium from active site to initiate the reaction in N146S-OG:AP$_{Ca\text{-}depleted}$ structures.

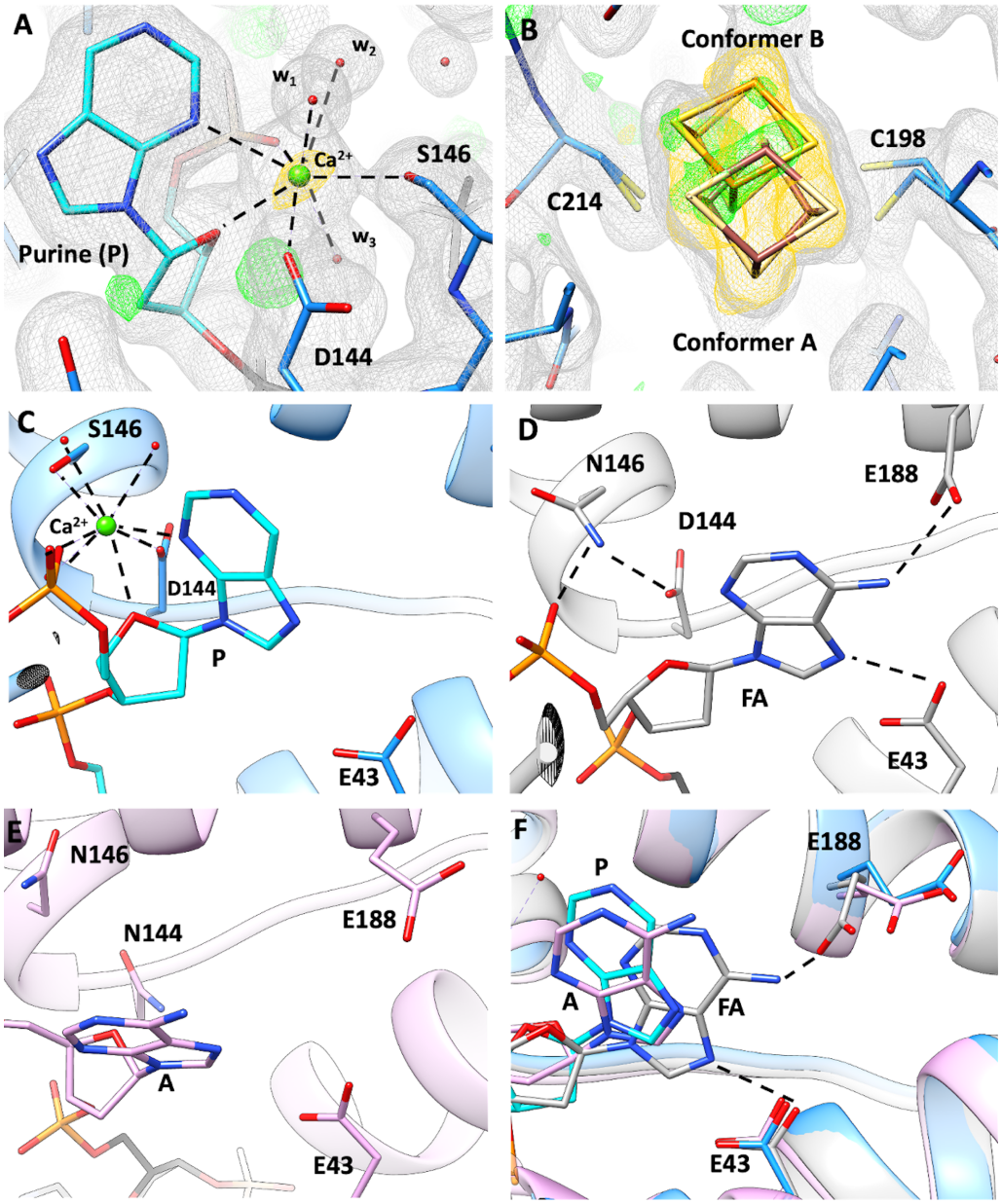

Figure 4 Structural overview of N146S Gs MutY-OG:P complex. (A) The final refinement map of N146S-OG:P. A Ca^{2+} ion coordination is observed with purine base and active site residues in N146S-OG:P complex structure. (B) Fe-S cluster with alternate conformations The $2|F_o| - |F_c|$ map (gray) was calculated to the 1.68 Å resolution limit and contoured at 1.0 rmsd. The $|F_o| - |F_c|$ map (green, positive features; red, negative) was contoured at 3.5 rmsd. The ANOM map contoured to 5.0 rmsd (gold). (C) N146S-OG:P complex structure with purine coordinated to Ca^{2+} and disengaged from Glu43. (D) Fluorinated Lesion Recognition Complex (FLRC) showing the interaction of active site residues and adenine (PDB ID:3G0Q, gray) (6). (E) Lesion Recognition Complex (LRC) showing adenine disengaged from Glu43 (PDB ID:1RRQ, light pink) (39). (F) The overlay of N146S-OG:P (cyan) with FLRC (PDB ID:3G0Q, gray) (6) and LRC (PDB ID:1RRQ, light pink) (39) presents base engagement in active site.

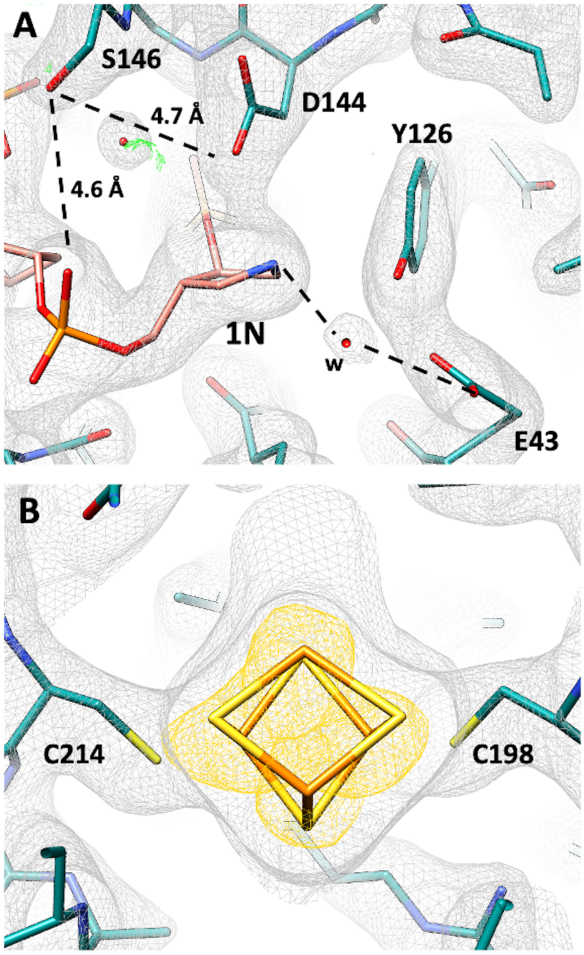

Figure 5 The structural overview of N146S-OG:1N. (A) Electron density maps for N146S-OG:1N showing chain A and C. The $2|F_o| - |F_c|$ map (gray) was calculated to the 1.96 Å resolution limit and contoured at 1.0 rmsd. The $|F_o| - |F_c|$ map (green, positive features; red, negative) was contoured at 3.5 rmsd. (B) The electron density map of iron-sulfur cluster with ANOM map contoured to 5.0 rmsd (gold).

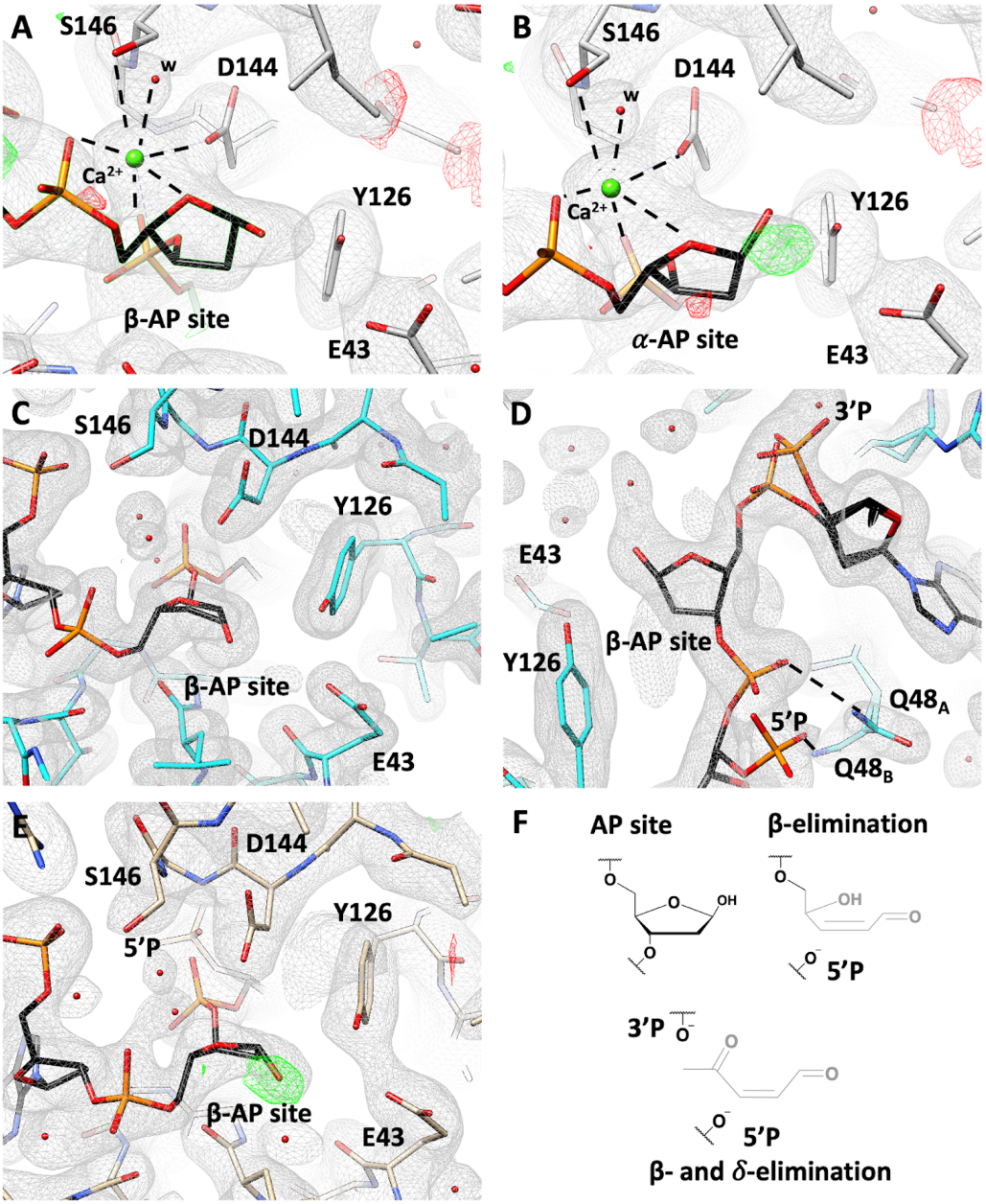

Figure 6 Structural overview of the three AP product structures. (A) The active site view of N146S-OG: $AP_{Ca\text{-}inhibited}$ shows Ca^{2+} coordination and β anomer AP product. The $2|F_o| - |F_c|$ map (gray) was calculated to the 2.36 Å resolution limit and contoured at 1.0 rmsd. The $|F_o| - |F_c|$ map (green, positive features; red, negative) was contoured at 3.5 rmsd. (B) Electron density features in the $|F_o| - |F_c|$ map indicate the α anomer is incompatible with measured diffraction data. (C) The active site view of N146S-OG:$AP_{Ca\text{-}free}$ with AP site product. (D) β- and δ-elimination products shown with alternate conformations of Q48 coordinating to the phosphate backbone conformations of G ($2|F_o| - |F_c|$ map contoured to 1.0 rmsd and $|F_o| - |F_c|$ map contoured to 3.5 rmsd) (E) N146S-OG:$AP_{Ca\text{-}depleted}$ structures with the β anomer AP product ($2|F_o| - |F_c|$ map contoured to 1.0 rmsd and $F_o| - |F_c|$ map contoured to 3.8 rmsd) and (F) Chemical structures of AP site, β-elimination and β- and δ-elimination products.

Supplementary Information

Structural snapshots of base excision by the cancer-associated variant MutY N146S reveal a retaining mechanism

Merve Demir,[1] L. Peyton Russelburg,[2] Wen-Jen Lin,[1] Carlos H. Trasvina-Arenas,[1] Beili Huang,[1] Phil K. Yuen,[1] Martin P. Horvath,[2,*] and Sheila S. David[1,*]

[1] Department of Chemistry, University of California, Davis, California, 95616, USA
[2] School of Biological Sciences, University of Utah, Salt Lake City, Utah, 84112, USA

* To whom correspondence should be addressed. Email: ssdavid@ucdavis.edu; martin.horvath@utah.edu

Supplementary Figures

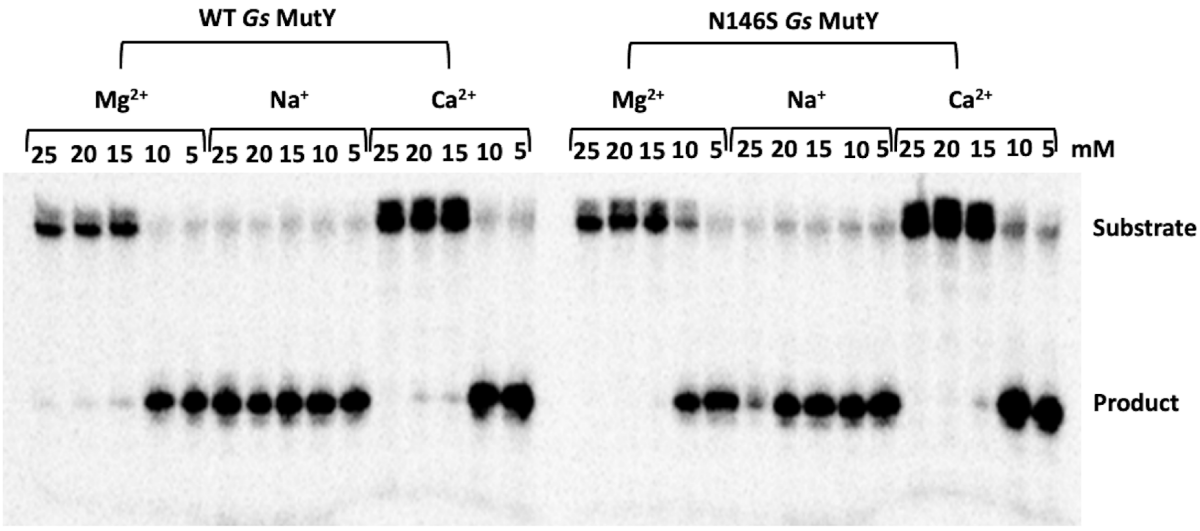

Figure S1 Metal ion inhibition of WT (120 nM) and N146S (100 nM) *Gs* MutY were evaluated using glycosylase assay under single turnover conditions with 20 nM radiolabeled OG:A containing DNA and including 5-25 mM concentrations of Mg^{2+}, Na^{+} and Ca^{2+}. Each reaction was quenched with NaOH after 60 minutes of incubation. The results showed no activity of WT or N146S with concentrations of divalent metals higher than 15 mM, while the activity was maintained in the presence of Na^{+}.

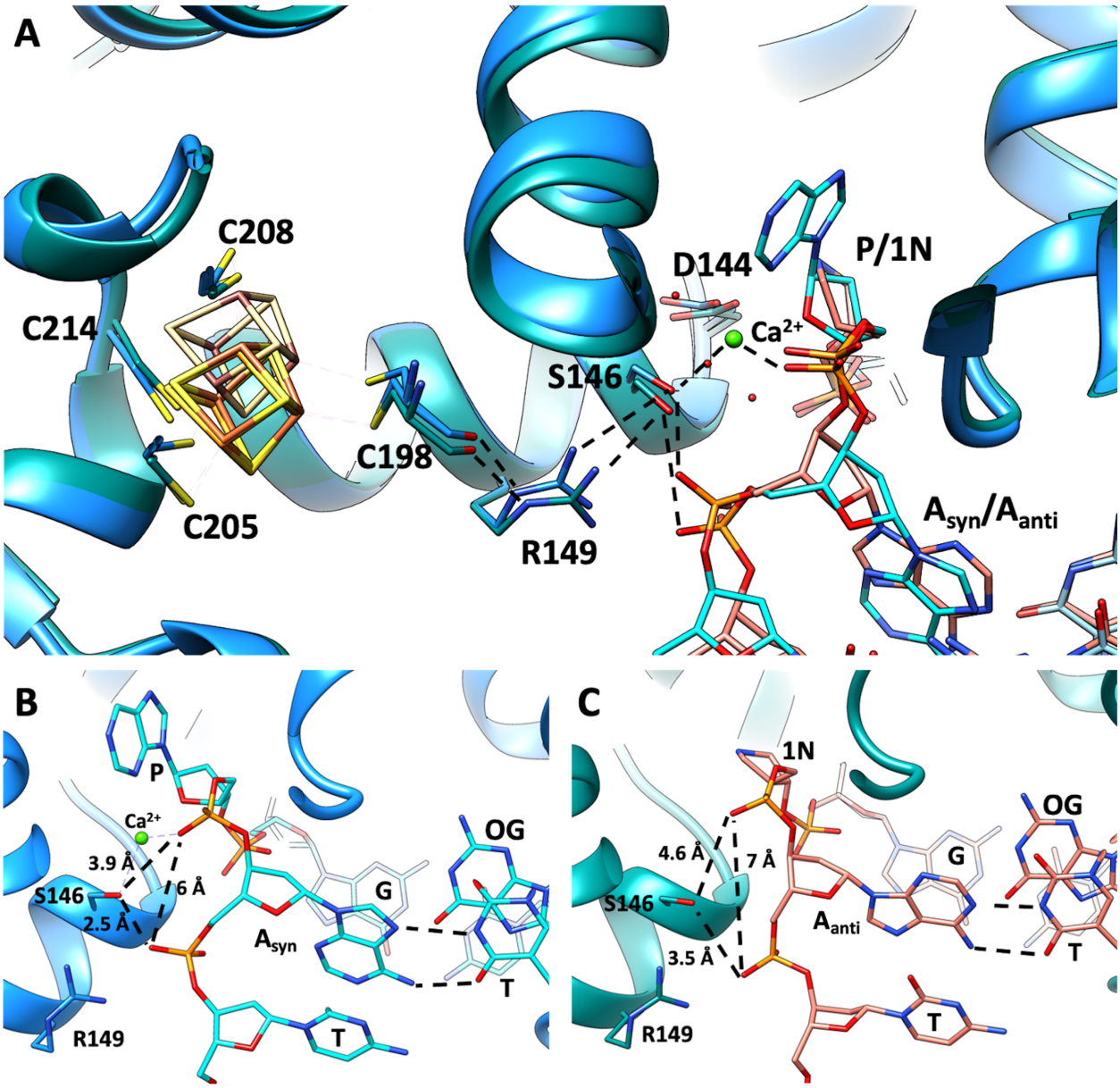

Figure S2 Overviews of neighboring A nucleotide and Fe-S cluster. (A) N146S-OG:P structure shows the adenine neighboring the purine base adopts a *syn* conformation. (B) The same adenine assumes the *anti* conformation in N146S-OG:1N structure. (C) The comparison of N146S-OG:P structure to N146S-OG1N (Chains A,B and C) shows conformational changes for adenine, S146, R149 and Fe-S cluster with coordinating cysteines.

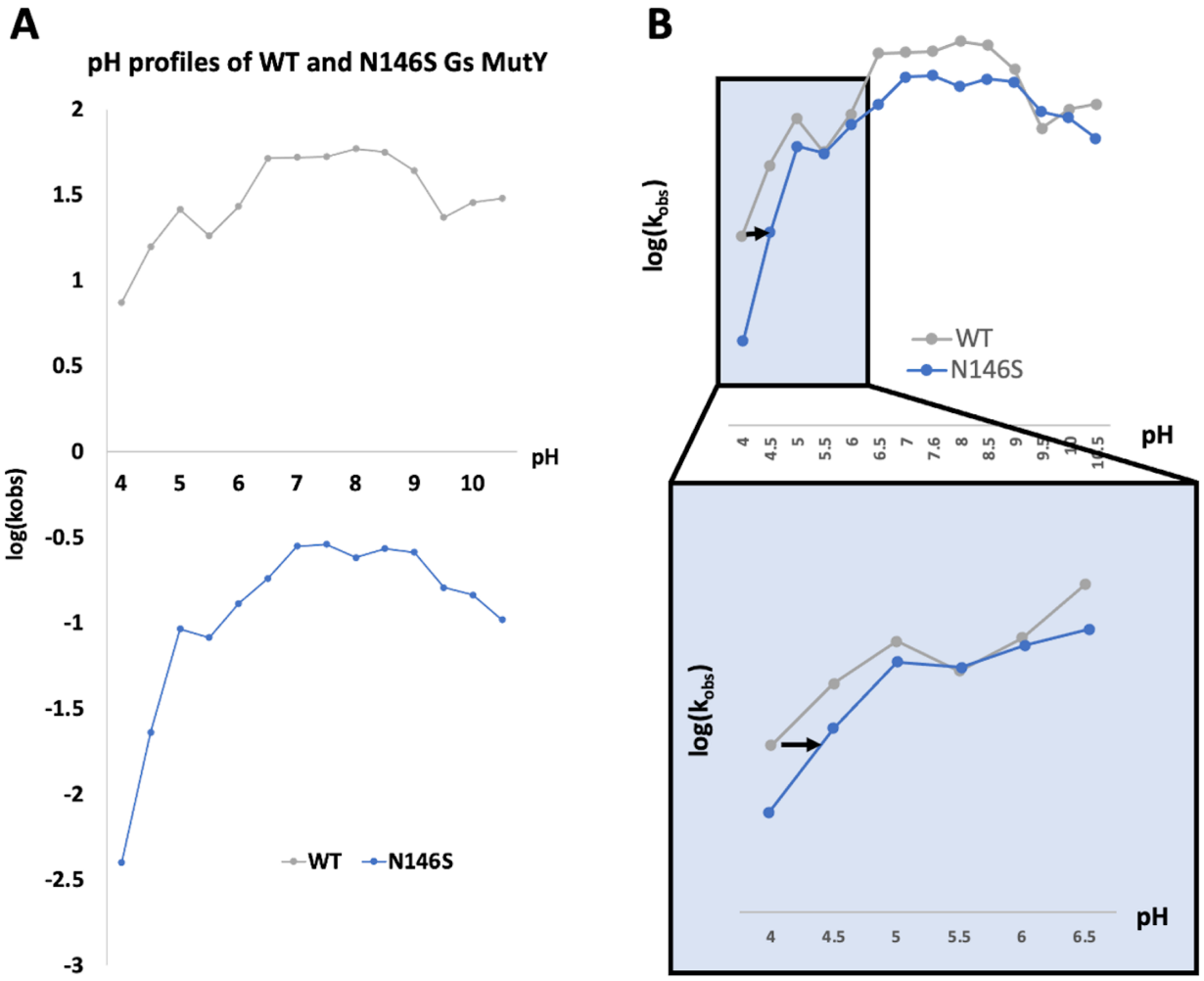

Figure S3 pH-dependence of adenine glycosylase activity with OG:A substrate duplex. (A) The pH profiles of WT and N146S *Gs* MutY with observed rates (k_{obs}) determined from at least three trials of glycosylase assay performed under single turnover conditions at each pH condition. The rate constants for pH range of 4-5 were estimated from the initial rates of the first three time points. (B) The overlaid curves of WT and N146 with a close-up view in pH range of 4 to 6.5.

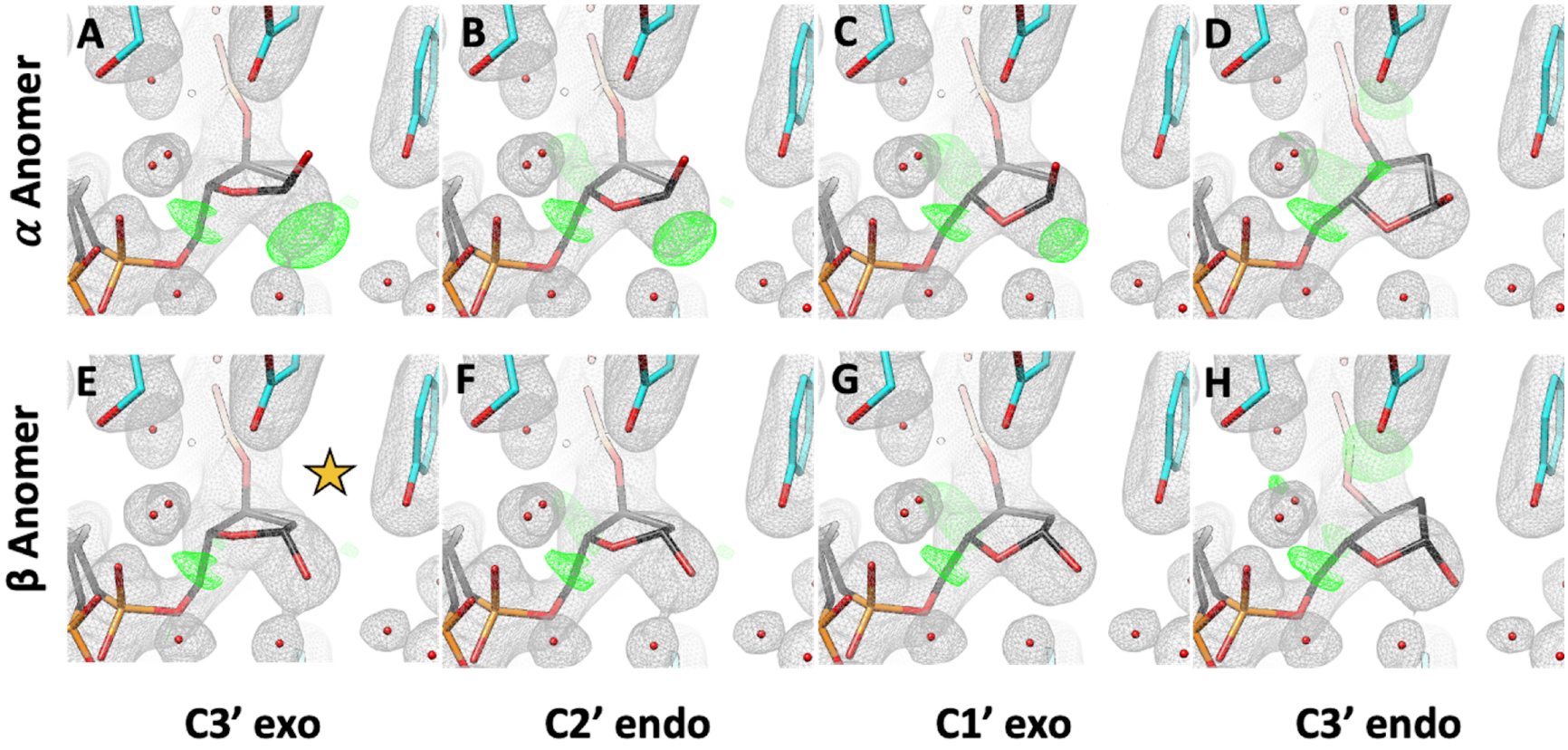

Figure S4 Abasic site models of N146S-OG:$P_{Ca\text{-}free}$. (A) The α anomer with 3-exo sugar pucker, (B) with 2-endo sugar pucker, (C) with 1-exo sugar pucker (D) and 3-endo sugar pucker. (E) The β anomer with 3-exo sugar pucker, (F) with 2-endo sugar pucker, (G) with 1-exo sugar pucker and (H) with 3-endo sugar pucker. $2|F_o| - |F_c|$ maps contoured to 1.1 rmsd and $|F_o| - |F_c|$ maps contoured to 3.8 rmsd. These maps technically get the modifier "maximum likelihood weighted", meaning the coefficients for $|F_o|$ and $|F_c|$ are further weighted by confidence in the data. The gold star on E shows the selected best fit for the electron density.

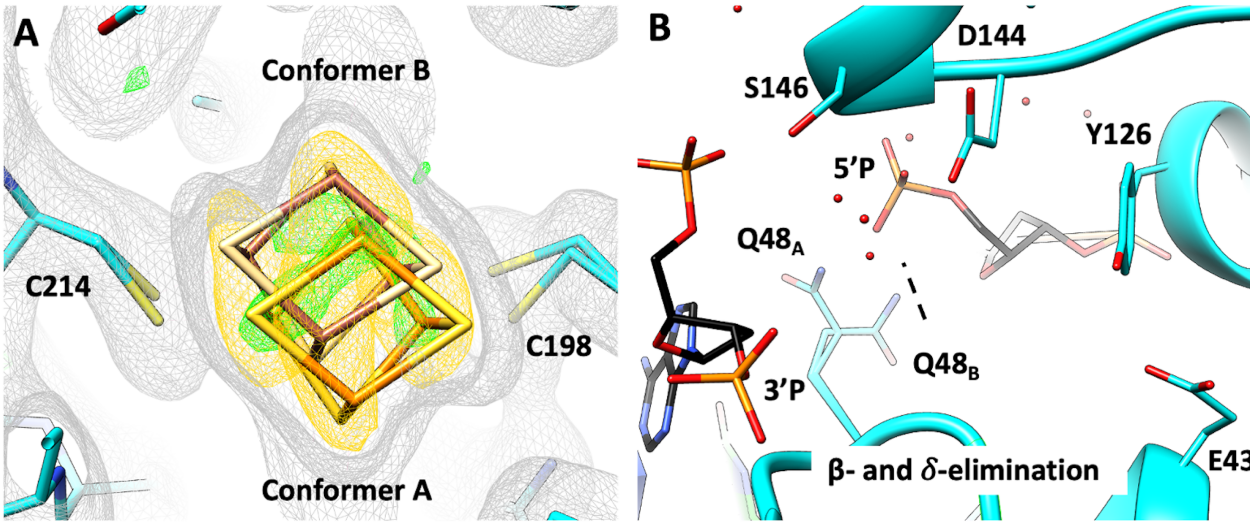

Figure S5 Alternate conformations in N146S-OG:$AP_{Ca\text{-}free}$ structure. (A) Active site of N146S-OG:$AP_{Ca\text{-}free}$ view of alternate conformations of Gln48 (B) Anomalous signal in gold contoured to 5.0 rmsd for Fe atoms in alternate conformations

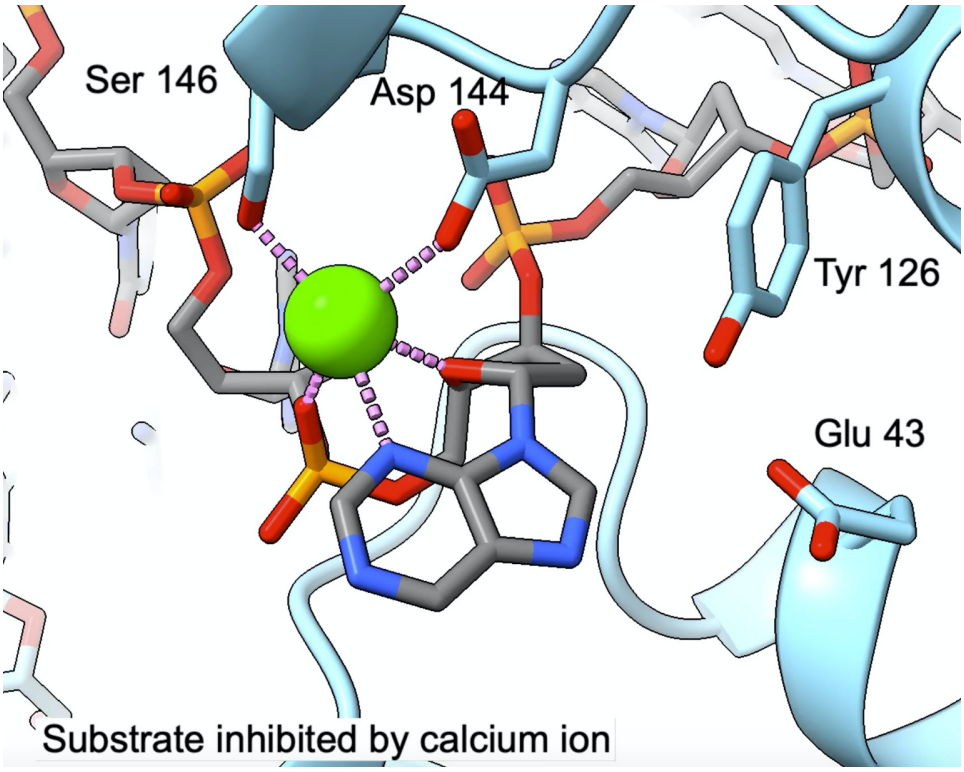

Movie S1 The structural movie of base excision by N146S *Gs* MutY. Calcium coordination at the active site disengages the base from Glu43. We believe removal of the calcium allows the base to take a conformation engaged with Glu43 for protonation and N-glycosidic bond cleavage as shown here by using the coordinates for the base engaged conformation from FLRC structure (1). An oxacarbenium ion intermediate is proposed to be formed and stabilized by Asp144 (2). The N146S-OG:1N structure mimics the transition state of the second step of the reaction with a water nucleophile activated by Glu43 that attacks C1 to form the β-anomer AP site product. Finally, our N146S-OG:AP structures provided the evidence for this retaining mechanism of MutY.

Table S1 Data collection statistics

Data collection	N146S-OG:P	N146S-OG:1N	N146S-OG:AP Ca Free	N146S-OG:AP Ca Inhibited	N146S-OG:AP Ca Depleted
PDB ID	8DVP	8DW7	8DW0	8DVY	8DW4
Wavelength (Å)	1.11585	1.11585	1.11585	0.97741	0.97741
Resolution range (Å) *	73.49 – 1.54	72.80 – 1.96	74.02 – 1.68	70.35 – 2.36	54.45 – 2.49
Highest resolution shell (Å)	(1.58 – 1.54)	(2.01 – 1.96)	(1.72 – 1.68)	(2.42 – 2.36)	(2.55– 2.49)
Space group	$P2_12_12_1$	$P2_1$	$P2_12_12_1$	$P2_12_12_1$	$P2_12_12_1$
Unit cell a (Å)	37.68	48.89	37.94	37.86	37.64
b (Å)	86.17	137.21	86.56	85.48	85.55
c (Å)	140.77	74.16	142.77	140.71	141.17
beta (°)	90.0	101.00	90.0	90.0	90.0
Total reflections	1,679,820	403,636	386,898	250,971	108,272
Unique reflections	130,827	128,636	101,188	36,236	30,778
Multiplicity	12.8	3.14	3.82	6.9	3.5
Completeness (%)	99.8 (98.5)	94.7 (93.5)	97.7 (98.4)	99.9 (99.6)	99.8 (99.9)
Mean I/sigma(I)	13.15 (0.47)	8.89 (0.46)	6.01 (0.68)	6.81 (0.65)	4.98 (0.61)
Wilson B-factor ($Å^2$)	37.0	50.9	41.2	65.6	56.1
R-merge (%)	7.5 (337.8)	6.8 (235.0)	11.8 (336.9)	23.7 (326.4)	18.8 (185.2)
R-rim (%)†	7.5 (337.8)	7.2 (252.7)	13.3 (421.2)	23.7 (340.8)	18.8 (191.6)
CC1/2 (%)	99.9 (14.6)	99.8 (10.2)	99.7 (11.6)	99.4 (13.5)	98.9 (17.1)

***** Statistics for the highest-resolution shell are shown in parentheses.

† Redundancy independent measure of R; see Diederichs,K. and Karplus,P.A. (1997) Improved R-factors for diffraction data analysis in macromolecular crystallography. Nat. Struct. Biol., 4, 269–275 (3).

Table S2 Model refinement statistics

Model refinement	N146S-OG:P	N146S-OG:1N	N146S-OG:AP Ca Free	N146S-OG:AP Ca Inhibited	N146S-OG:AP Ca Depleted
Reflections	130279	127732	100899	36226	30761
R-work	0.2172	0.2030	0.1999	0.2474	0.2311
R-free	0.2327	0.2343	0.2266	0.2738	0.2488
Atoms, non-hydrogen	3330	6429	3414	3143	3158
MutY	2694	5352	2759	2681	2680
DNA	431	844	447	426	435
OG nucleotide	23	46	23	23	23
Active site nucleotide	20	22	17	12	13
Calcium	3	2	N.A.	3	N.A.
Fe4S4	16	16	16	8	8
Solvent	182	191	188	24	31
RMSD bonds (Å)	0.014	0.020	0.016	0.007	0.003
RMSD angles (°)	1.291	1.463	1.324	0.904	0.633
Ramachandran favored (%)	96.0	97.5	98.3	97.1	97.7
allowed (%)	4.0	2.5	1.7	2.9	2.3
outliers (%)	0.00	0.00	0.0	0.00	0.00
Rotamer outliers (%)	0.00	0.96	0.00	0.00	1.51
Clashscore	1.84	1.86	2.43	2.54	2.53
Average B non-H ($Å^2$)	46.6	57.2	46.8	61.7	59.9
MutY ($Å^2$)	47.9	60.3	48.1	61.8	60.4
DNA ($Å^2$)	40.6	46.8	40.4	61.6	58.3
OG nucleotide ($Å^2$)	25.1	38.7	24.7	44.0	38.3
Active site nucleotide ($Å^2$)	30.2	41.6	36.6	67.9	38.5
Calcium ($Å^2$)	42.5	39.6	N.A.	58.0	N.A.
Fe4S4 ($Å^2$)	34.4	50.7	34.6	49.3	53.8
Solvent ($Å^2$)	42.0	48.7	43.5	53.1	42.3

Works Cited

1. Lee,S. and Verdine,G.L. (2009) Atomic substitution reveals the structural basis for substrate adenine recognition and removal by adenine DNA glycosylase. *Proc. Natl. Acad. Sci.*, **106**, 18497–18502.
2. Woods,R.D., O'Shea,V.L., Chu,A., Cao,S., Richards,J.L., Horvath,M.P. and David,S.S. (2016) Structure and stereochemistry of the base excision repair glycosylase MutY reveal a mechanism similar to retaining glycosidases. *Nucleic Acids Res.*, **44**, 801–810.
3. Diederichs,K. and Karplus,P.A. (1997) Improved R-factors for diffraction data analysis in macromolecular crystallography. *Nat. Struct. Biol.*, **4**, 269–275.